Ore Geology Reviews 156 (2023) 105405

Contents lists available at ScienceDirect

Ore Geology Reviews

journal homepage: www.elsevier.com/locate/oregeorev

A tool for Zn-Pb MVT exploration by combining C and O isotopes and REE geochemistry of dolomite

Dídac Navarro-Ciurana [a,b,*], Isaac Corral [a], Mercè Corbella [a]

[a] Departament de Geologia, Facultat de Ciències, Universitat Autònoma de Barcelona (UAB), Edifici Cs s/n, 08193 Bellaterra (Cerdanyola del Vallès), Spain
[b] Grup MAiMA, SGR Mineralogia Aplicada, Geoquímica i Hidrogeologia, Facultat de Ciències de la Terra, i Institut de Recerca de l'Aigua (IdRA), Universitat de Barcelona (UB), c/ Martí i Franquès s/n, 08028 Barcelona, Spain

ARTICLE INFO

Keywords:
Stable isotopes
Sr ratios
Rare earth element geochemistry
Exploration tool
Mississippi Valley-Type deposits
Fertile/barren hydrothermal dolomite

ABSTRACT

An exploration guide for Mississippi Valley-type (MVT) deposits is proposed and illustrated in the Riópar area (SE Spain), where extensive dolostone geobodies hosting Zn-(Fe-Pb) MVT mineralization occur. These base metal deposits are found within stratabound and patchy dolostones replacing Upper Jurassic to Lower Cretaceous limestones. However widespread stratabound dolostones, with no Zn-(Fe-Pb) mineralization associated, are also found in the same area replacing Lower Jurassic to Upper Cretaceous carbonates. A detailed sampling of both, Zn-(Fe-Pb) mineralized dolostones (fertile), as well as unmineralized ones (barren), has been performed in an area of ~106 km^2 to characterize their rare earth element (REE) and isotopic (C, O, Sr) compositions. Barren Lower and Middle Jurassic and Upper Cretaceous dolostones show C, O and Sr isotopic characteristics ($\delta^{13}C$ = +2.1 to +3.8‰ VPDB, $\delta^{18}O$ = +27.6 to +29.8 ‰ VSMOW, $^{87}Sr/^{86}Sr$ = 0.70736 to 0.70764) like the Jurassic-Cretaceous undolomitized limestones and marine carbonates, and consistent with dolostones produced by low temperature seawater. On the contrary, barren and fertile Upper Jurassic to Lower Cretaceous stratabound and patchy dolomitized limestones are depleted in $\delta^{13}C$ and $\delta^{18}O$ and relatively enriched in $^{87}Sr/^{86}Sr$ compared to the host limestones. This $\delta^{13}C$ and $\delta^{18}O$ composition can be explained by an interaction of warm fluids with regional carbonates (2–3% of fluid/rock interaction at 190–230 °C). The hydrothermal character for the dolomitizing fluid is supported by REE geochemical data (e.g., $(Pr/Pr^*)_{PAASN}$ and $(Ce/Ce^*)_{PAASN}$ anomalies). Thus, C and O isotopes, as well as $(Ce/Ce^*)_{PAASN}$ and $(Pr/Pr^*)_{PAASN}$ ratios, can be used to discriminate between low temperature dolostones, formed from cold seawater that do not contain Zn-(Fe-Pb) mineralization (barren), from hydrothermal dolomites (HTDs), which may host Zn-(Fe-Pb) mineralization. Furthermore, most barren HTDs show more restricted and higher $\delta^{13}C$ (+0.4 to +0.9 ‰ VPDB) and $\delta^{18}O$ values (+26.4 to +27.1 ‰ VSMOW), as well as lower $\sum$REE contents (5.41 to 7.38 mg kg^{-1}), compared to Zn-(Fe-Pb) mineralized HTDs ($\delta^{13}C$: −2.3 to +0.6 ‰ VPDB; $\delta^{18}O$: +25.1 to +27.1 ‰ VSMOW; $\sum$REE 14.10 to 54.79 mg kg^{-1}). Therefore, the obtained REE contents, and partially the $\delta^{13}C$ values, can be used to discriminate between HTDs associated with Zn-(Fe-Pb) mineralization (fertile dolostones) and barren HTDs, revealing their potential as a new geochemical tool for MVT exploration in dolomitized terrains.

1. Introduction

The study of dolostones and dolomitizing processes is of a great interest as the resulting rocks may host economic Zn-Pb-F ore deposits (i.e., Mississippi Valley-Type, MVT, and Sedimentary Exhalative, SEDEX; Leach and Sangster, 1993; Muchez et al., 2005), as well as more than half of the world's hydrocarbon reserves (e.g., Zenger et al., 1980; Warren, 2000; Davies and Smith, 2006). Of the many trace elements commonly found in sphalerite, which is the main economic mineral in MVT, SEDEX and Irish-type Zn-Pb deposits, gallium (Ga), germanium (Ge) and indium (In) are currently the most relevant (Schwarz-Schampera and Herzig, 2002; Cook et al., 2009, 2011; Marsh et al., 2016; Frenzel et al., 2016; Sahlström et al., 2017a, Sahlström et al., 2017b). These metals have become increasingly coveted in recent years largely due to their growing usage in smartphones (Ga, In), fiber-optic cables (Ge) or solar cells (Ga, Ge, In; Guberman, 2015; Jaskula, 2015; Tolcin,

* Corresponding autor at: Departament de Geologia, Facultat de Ciències, Universitat Autònoma de Barcelona (UAB), Edifici Cs s/n, 08193 Bellaterra (Cerdanyola del Vallès), Spain.
E-mail address: didac.navarro@uab.cat (D. Navarro-Ciurana).

https://doi.org/10.1016/j.oregeorev.2023.105405
Received 13 December 2022; Received in revised form 19 March 2023; Accepted 19 March 2023
Available online 22 March 2023

2015). The rapid increase in their economic importance as well as supply concerns are reflected in their recent identification as critical raw materials (Erdmann and Graedel, 2011; EU Commission, 2020).

Dolostone formation has been linked with different geological processes and settings (Machel, 2004) and various dolomitization models have been proposed by a large number of workers (e.g., Warren, 2000 and references therein). From the ore deposits perspective, dolostones can be broadly classified as: i) low temperature dolostones, formed from cold Mg-rich seawater derived fluids (SWDs) that are unrelated to economic Zn-Pb-F deposits; and ii) hydrothermal dolomites (HTDs), formed at slightly to much higher temperatures by seawater derived fluids or by other Mg-bearing fluids; both with similar macroscopic characteristics. HTDs are commonly structurally controlled and can host Zn-Pb-F mineralization (e.g., Boni et al., 2000; Duggan et al., 2001; Davies and Smith, 2006; Gasparrini et al., 2006; Smith and Davies, 2006; Sharp et al., 2010). The HTD geobodies result in a variety of geometries, but the most common are: i) stratabound and tabular-shaped dolostones which extend away from fault zones following suitable layers (e.g., Sharp et al., 2010; Lapponi et al., 2011; Martín-Martín et al., 2013; Dewit et al., 2014; Rahim et al., 2022); ii) fault-related irregular dolostones distributed in patches along fault traces (e.g., Duggan et al., 2001; Wilson et al., 2007; López-Horgue et al., 2010; Rahim et al., 2020); and iii) Christmas-tree like morphology, that results from combination of stratabound and patchy end-members in individual dolostone bodies (e.g., Sharp et al., 2010). Nevertheless, low temperature dolostones may also form stratabound geometries (e.g., Hirani et al., 2018), so that the geometry or their appearance cannot be used as exploration criteria for finding MVT-related mineralization.

Dolostones are usually classified according to dolomite crystal size, texture, fabric, distribution and shape (Friedman, 1965; Randazzo and Zachos, 1984). Gregg and Sibley (1984) and Sibley and Gregg (1987) proposed a classification of dolomite textures according to crystal growth effects (planar or non-planar) and the degree of dolomitization based on their formation temperature. Planar dolomite is assumed to precipitate during early diagenesis at temperatures around or lower than 50–60 °C in shallow-burial environments (Machel, 2004). On the other hand, the precipitation of non-planar dolomite usually occurs at higher temperatures than 50–60 °C, commonly under deep-burial diagenetic conditions (Warren, 2000). Also, non-planar saddle dolomite, characterized by curved crystal faces and wavy extinction, is interpreted to precipitate from hydrothermal fluids under a temperature range from 80 to 150 °C and exceptionally up to 200 °C (Machel, 2004). Nevertheless, evidence from microthermometric data of fluid inclusions (FIs) from non-planar dolomites constituting Zn-Pb mineralized and barren dolostones of varied ages and locations do not support this view (e.g., Grandia et al., 2003; Nader et al., 2004; Luczaj, 2006; López-Horgue et al., 2010; Poros, 2011; Ronchi et al., 2012; Martín-Martín et al., 2013, 2015; Gomez-Rivas et al., 2014; Hao et al., 2014; Huang et al., 2014; Navarro-Ciurana et al., 2015, Navarro-Ciurana et al., 2016a). Thus, dolomite textures cannot be used as a quick and handy tool to determine their formation temperature and their possible link to MVT mineralization. Furthermore, assigning a diagenetic environment of formation (deep-burial versus shallow-burial) based exclusively on textural descriptions can also result in misleading interpretations. Hydrothermal dolomitizing fluids, usually generated at depth, may ascend through fractures or faults, and evolve through interaction with host rocks, reaching shallow burial environments being able to maintain its high temperature or salinity. Although microthermometric studies of FIs in dolomites allow to determine their temperature of precipitation, and consequently, their hydrothermal origin, the processing time of this technique and the difficulty to find suitable dolomites, very often delays the exploration process. Therefore, exploration companies commonly decline the use of FIs and microthermometry in the early stages of exploration.

A large number of dolostone case studies were based on detailed petrographic descriptions, geochemical analyses of trace elements and rare earth elements (REE), as well as on the isotopic compositions (C, O, Sr), to unravel dolomitization processes. Carbon and oxygen isotope composition from unaltered limestone to high-grade ores have been used to map the extent of hydrothermal systems, to understand fluid-rock interactions and have provided useful guides for the exploration of hydrothermal deposits worldwide (Banner et al., 1988; Naito et al., 1995; Vázquez et al., 1998; Large et al., 2001; Bierlein et al., 2004; Kelley et al., 2006). But contrary to other deposit types such as porphyry copper, high sulfidation epithermal, volcanic-hosted massive sulfide, Carlin-type Au or Irish-type Zn-Pb deposits, where whole-rock and stable isotope geochemical tools, and mineral vectors have been developed (e.g., Chang et al., 2011; Barker et al., 2013; Loucks, 2014; Wilkinson et al., 2015; Lu et al., 2016: Richards, 2016; Corral et al., 2017; Tan et al., 2017; Yesares et al., 2019; Behnsen et al., 2021; Gisbert et al., 2021), this have been partially overlooked for MVT deposits. Instead, general, and large-scale guidelines for exploration have been proposed (e.g., Large et al., 2001; Leach et al., 2005; Wilkinson, 2014), although efforts have been applied to constrain lithogeochemical zonation sequences with some elements (Bi, Sb, Pb, Cd, Zn, among others: Hosseini-Dinani and Aftabi, 2016 and references therein). Therefore, during early stages of MVT exploration it is critical to effectively identify HTDs that are associated with Zn-Pb-F mineralization.

The Riópar area (Prebetic Cordillera, SE Spain) contains dolostone bodies of different ages, dimensions, and origins, as well as Zn-(Fe-Pb) MVT deposits which were mined since the XVIII century (Navarro-Ciurana et al., 2016a,b, 2017). According to Navarro-Ciurana et al. (2016a), the host dolostones of the Riópar mineralization consist of two stratabound dolostone bodies connected by patchy bodies, which replace carbonate units of Upper Jurassic to Lower Cretaceous ages. The dolomitizing fluid in the mineralized area resulted from the interaction of a hydrothermal brine and the carbonate host at temperatures between 150 and 250 °C (Navarro-Ciurana et al., 2016a). Nevertheless, other extensive dolostone geobodies also occur in the sedimentary record of the area, from Lower Jurassic to Upper Cretaceous strata, which have never been studied nor prospected, providing a great opportunity to compare mineralized (fertile) and non-mineralized (barren) dolostones. Therefore, stable isotopes (C, O), Sr isotopic ratios and REE data from the Riópar dolostones are presented in this study to illustrate their potential as a new exploration guide for MVT deposits, providing a valuable opportunity to test the proposed geochemical tool to discriminate Zn-(Fe-Pb) mineralized (fertile) from barren dolostones.

1.1. Geological setting

The Riópar area is located in the External Zones of the Betic Cordillera (SE Spain), which constitutes the westernmost part of the Mediterranean Alpine chain, together with the Rif in northern Morocco and Tell-Kabylies Ranges in northern Algeria (e.g., Sanz de Galdeano, 1990; Fig. 1). The External Zones (subdivided into the Prebetic and Subbetic zones; Fig. 1), are defined as an NNW-verging fold-and thrust belt of the Betic orogen, consisting of Mesozoic to Cenozoic marine sediments, originally deposited in the southern part of the Iberian continental paleomargin (e.g., García-Hernández et al., 1980; Sanz de Galdeano, 1990; Vera et al., 2004). The Prebetic Zone consists of Mesozoic to Cenozoic carbonates and clastic sequences up to 2000 m thick, which were folded and detached from the Paleozoic basement along Upper Triassic sedimentary rocks during the main orogenic stage in the Miocene (Barbero and López-Garrido, 2006; Vilas et al., 2001).

The tectonic evolution of the Mesozoic basin in the Prebetic margin started in Late Permian-Early Triassic age with an intracontinental rifting (Fig. 2) related to the opening of the Tethys Ocean and to the dismembering of the Pangea supercontinent by the divergence of the European and African plates (Banks and Warburton, 1991; Barbero and López-Garrido, 2006). This initial phase, represented by deposition of the "Germanic" facies (Buntsandstein, Muschelkalk, and Keuper), was followed by a post-rifting stage during the Early to Middle Jurassic

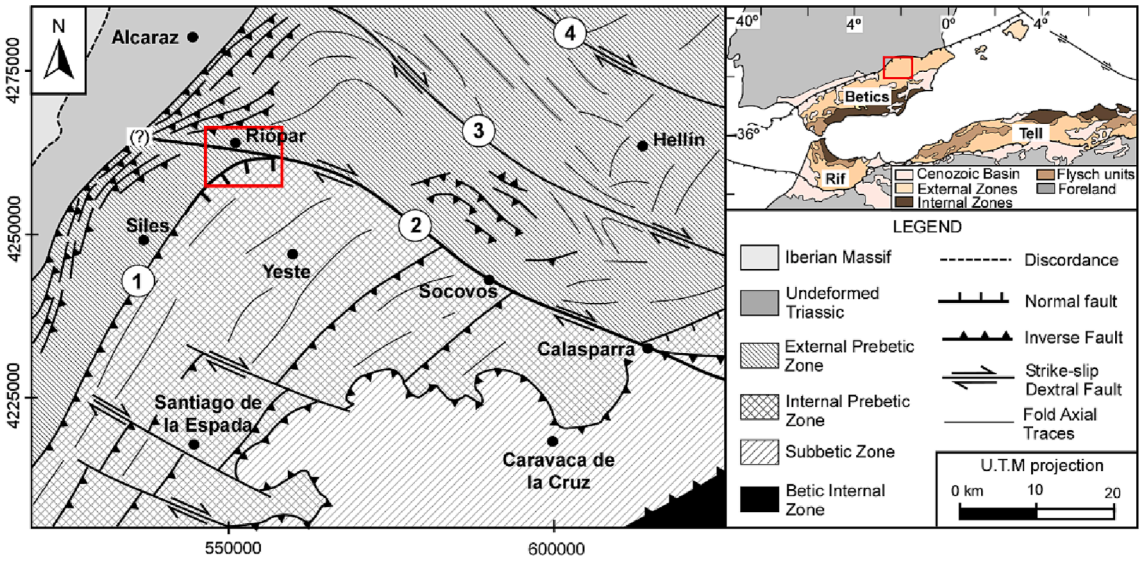

Fig. 1. Schematic geologic map of the Prebetic Zone and Riópar area (modified from: Pérez-Valera et al., 2010): (1) Alto Guadalquivir-San Jorge fault; (2) Socovos fault; (3) Liétor fault; and (4) Pozohondo fault.

(Fig. 2) with development of regional thermal subsidence, little fault activity and shallow carbonate platforms (García-Hernández et al., 1980). A Late Jurassic-Early Cretaceous rifting cycle, related to the opening of the North Atlantic Ocean by the break-up of Iberian and African plates, lead to the separation of the Prebetic domain from the rest of the Betic basin, and also from the rest of the Iberian Plate (Fig. 2; Banks and Warburton, 1991; Arias et al., 1996; Vilas et al., 2001). A post-extensional thermal subsidence stage occurred during Late Cretaceous ages (Fig. 2) with the development of extensive shallow-marine carbonate platforms in the Iberian margins. The destruction of the Prebetic margin was due to the rise of the Betic Chain, which started in the Paleogene, although the main collision event occurred during the Miocene (Fig. 2) as a consequence of the convergence of the African and Iberian plates (Barbero and López-Garrido, 2006).

The Prebetic domain is separated by major faults in the External and Internal Prebetic Zones (Fig. 1); the Riópar old mining area, which has the oldest brass processing plant of Spain, is located at the limit of these two zones (Fig. 1). From a tectonic standpoint, the Prebetic Zone is characterized by the Cazorla-Alcaraz-Hellín structural arc, which was developed during the Middle to Upper Miocene (Rodríguez-Pascua et al., 2000; Fig. 1). It consists of a set of NE-trending and SE-dipping faults and NW-trending strike-slip dextral faults perpendicular to the arc fold axes (Rodríguez-Estrella, 1979; Fig. 1). The NE-trending Alto Guadalquivir-San Jorge and Socovos-Calasparra faults separate the External (to the S) and the Internal (to the N) Zones (Fig. 1). The External Prebetic Zone (Fig. 1), dominated by shallow internal platform facies, corresponds to the deformed part of the septentrional basin where frequent stratigraphic gaps are observed. This zone contains well exposed Triassic, Jurassic and some Cretaceous and Paleogene sedimentary rocks. Furthermore, the External Prebetic Zone consists of an imbricate reverse fault structure with narrow overturned folds, overthrusting towards the central Spanish plateau. The Internal Prebetic Zone, located basinwards or to the South, is dominated by marginal platform to slope facies and large fold and thrust structures with no Triassic rocks, scarcity of Jurassic strata and extensively exposed Cretaceous and Paleogene sedimentary rocks, which are overthrusted by Subbetic nappes (Fig. 1; Azéma, 1977; Barbero and López-Garrido, 2006; García-Hernández et al., 1980; Vera et al., 2004).

1.2. Characteristics of the Riópar MVT mineralization

The Riópar Zn-(Fe-Pb) Mississippi Valley-type (MVT) mineralization, located in the limit between External and Internal Prebetic Zones, is hosted exclusively in stratabound and patchy dolostones of the Upper Member (Mb.) of Sierra del Pozo Formation (Fm.) (Figs. 2 and 3). According to Navarro-Ciurana et al. (2016b), the Riópar deposits, which were mined since 1773, produced a minimum of ~ 20,000 t of Zn along its mining history. Five sulfide orebodies have been recognized along a 1.6 km WE-trending normal fault alignment (Fig. 4) with approximate dimensions of 20–50 m (height), 50–100 m (length) and 20–30 m (width; Navarro-Ciurana et al., 2016b, 2017). The main Zn-(Fe-Pb) mineralization is distributed in two mining complexes (Fig. 4): i) San Agustín, which consists of two ore bodies named “Sg1” and “Sg2”; and ii) San Jorge, situated in the central part of the studied area, which contains different small ore bodies, which are grouped in three mines (Sj1, Sj2, Sj3).

The Zn-(Fe-Pb) sulfide deposits are distributed along the footwall block of the WE-trending and S-dipping San Jorge extensional fault (SJF). The associated hydrothermal dolomitization (fluid inclusion homogenization temperatures around 205 °C: Navarro-Ciurana et al., 2015, 2016a) is limited by the NW-trending Socovos fault (SF) (Figs. 3 and 4). The SJF seems to have focused the hydrothermal dolomitizing and ore-bearing fluids, indicating a structural control for fluid flow. The Upper Jurassic to Lower Cretaceous succession does not crop out in the hanging block of the San Jorge fault; it cannot be confirmed if this zone was affected by the same dolomitizing and mineralizing processes (Navarro-Ciurana et al., 2016b). Most of the deposits in this area are characterized by an extensive supergene alteration due to weathering of the hypogene Zn-Fe-Pb sulfides, resulting in the formation of supergene non-sulfide (“calamine”) mineralization (Fig. 5a). The hypogene mineralization, which mainly consists of sphalerite, marcasite and galena (Fig. 5b), occurs in a variety of forms that include: i) NW- and NE-trending irregular lenses, dipping 20–50° to the south, forming cockade textures and in some cases crosscutting the stratification (Fig. 5a); ii) small branching bodies parallel to stratification connected to the irregular lenses; iii) ore-cemented breccia zones (Fig. 5c); iv) cm- to mm-wide veins and veinlets (Fig. 5d); and v) dissemination and stylolite porosity filling within the host dolomites. The hypogene mineral paragenesis consists of (Navarro-Ciurana et al., 2016a,b, 2017): i) early dolomite, with transitions of planar-s (subhedral) replacive (ReD) and planar-e (euhedral) light sucrosic (SuD) dolomite types (Fig. 5d); ii) early non-planar saddle dolomite (SaD-I) (Fig. 5d); iii) Zn–(Fe–Pb) ores composed of marcasite, sphalerite and minor galena (Fig. 5); iv) late non-planar saddle dolomite (SaD-II) (Fig. 5d); and v) late dolomite

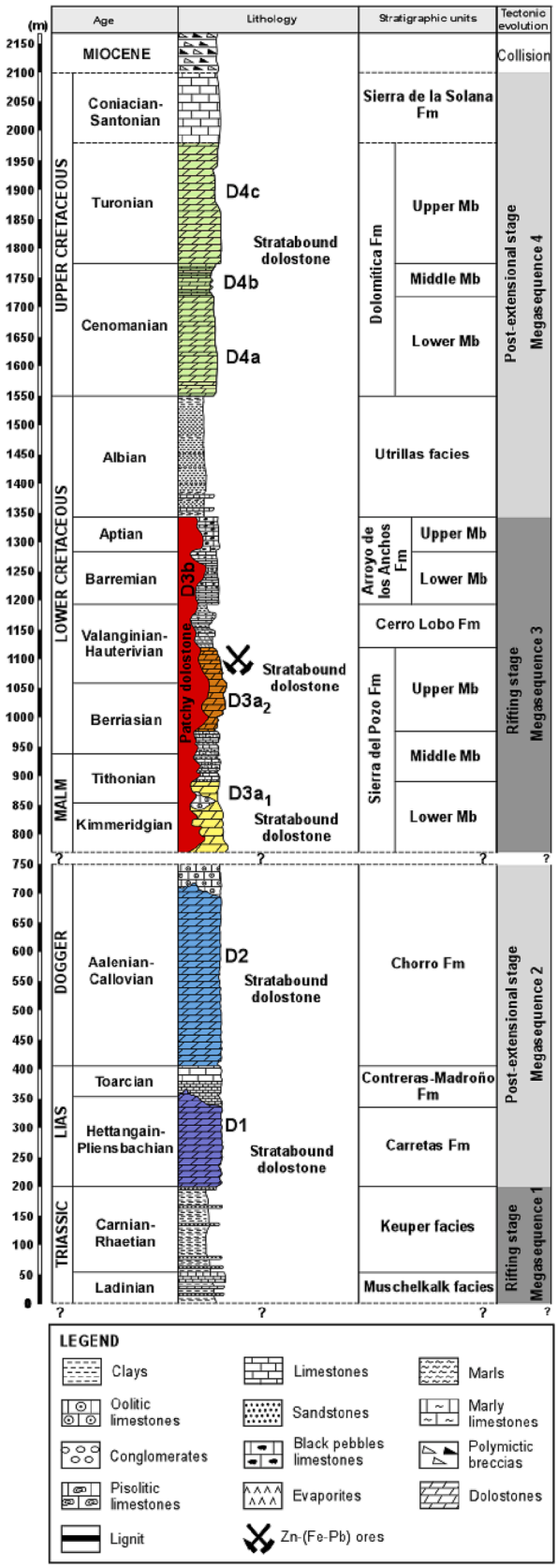

Fig. 2. Stratigraphic section of the Riópar area with sedimentary units and sequences, location of the studied dolostones and the Zn-(Fe-Pb) ores, with the tectonostratigraphic stages of the Prebetic Zone.

which consists of planar-e porphyrotopic (PoD) crystals replacing sphalerite (Fig. 5f). Furthermore, two successive stages of supergene ore formation under meteoric fluid processes occurred affecting hypogene mineralization: i) "gossan" and "red calamine" formation in the uppermost parts of the ore with deposition of Fe-(hydr)oxides and Zn- and Pb-carbonates (smithsonite and cerussite), occurring as direct replacements of Zn-Fe-Pb sulfides (Fig. 5a); and ii) "gray calamine" ore formation with deposition of smithsonite, cerussite and hydrozincite infilling microkarst cavities and porosity.

1.3. Sampling and analytical methods

A systematic sampling of carbonates was performed in an area of ~ 106 km^2 through the stratigraphic succession shown in Fig. 2, considering the different dolostone and limestone body types and ages, including surface and underground old mine workings. Representative polished thin sections (n = 202) of the different dolostone body types and limestones outcropping in the Riópar area (Fig. 3) were studied in detail using petrographic microscopy. Selected thin sections were previously half stained with alizarin red-S and K-ferricyanide to differentiate ferroan/non-ferroan dolomite and calcite (Dickson, 1966).

Oxygen, carbon and strontium isotope analyses were performed on regional Jurassic to Cretaceous limestones, as well as on the different outcropping dolostone bodies. Individual crystals were carefully manually microdrilled from polished slabs or alternatively handpicked under a binocular microscope considering the dolomite crystal type (planar-s replacive, planar-e replacive, planar-e sucrosic and non-planar saddle dolomites; Table 1) and powdered. Furthermore, some representative samples were isotopically analyzed as whole rock (O, C and Sr) to compare with minor and trace element crystal compositions (Table 1).

O and C isotope compositions (n = 121) were analyzed at Centres Científics i Tecnològics of the Universitat de Barcelona (CCiTUB). About 0.05 to 0.08 mg of sample were reacted at 70 °C with 100% phosphoric acid in a Thermo Finnigan Kiel Device III, coupled online with a Thermo Finnigan MAT-252. The carbon and oxygen isotopic ratios are reported in the delta notation: $\delta = (R_{sample} - R_{standard})/R_{standard} \times 1000$ (‰) with $R = {}^{13}C/{}^{12}C$ or ${}^{18}O/{}^{16}O$, where the results are referenced to the Vienna Pee Dee Belemnite (VPDB) standard. However, the $\delta^{18}O$ values listed in this paper are referenced to the Vienna Standard Mean Ocean Water (VSMOW). The relationship between VPDB and VSMOW is expressed as: $\delta^{18}O_{VSMOW} = 1.03091\ \delta^{18}O_{VPDB} + 30.91$ (Coplen et al., 1983). Laboratory standards were calibrated relative to the international standard NBS-18 ($\delta^{13}C$ = -5.01‰ and $\delta^{18}O$ = –23.2‰ VPDB) and NBS-19 ($\delta^{13}C$ = +1.95‰ and $\delta^{18}O$ = -2.2‰ VPDB). Reproducibility, determined by replicate analysis of standards, was better than ± 0.02‰ for carbon and ± 0.06‰ for oxygen.

$^{87}Sr/^{86}Sr$ ratios of carbonates (n = 36) were determined with an automated multicollector TIMS-Phoenix® mass spectrometer at the Geochronology and Isotope Geochemistry Centre of the Universidad Complutense de Madrid. Carbonate powder was dissolved in 5 mL of 0.5 M acetic acid. Once dried, 1 mL of 3 M HNO_3 was added to the sample and dried again. 3 mL of 3 M HNO_3 were then added to the samples, which were subsequently centrifuged at 4000 r.p.m. during 10 min in order to eliminate the solid residue (clay minerals, quartz, etc.). For the Sr chromatographic separation, an extraction resin SrResinTM (Trisken International) was employed. The Sr was recovered with 0.05 M HNO_3 as eluent. The fraction in which Sr was concentrated was recovered and dried for analyzing in the mass spectrometer. Sr analyses have been corrected for possible interference of ^{87}Rb and they have been normalized to the value $^{88}Sr/^{86}Sr = 0.1194$. Analytical precision was monitored by analysis of the NBS 987 standard (mean = 0.710246 (n = 6); 2σ = 0.000012). Analytical uncertainties (2σ) were 0.01% for $^{87}Sr/^{86}Sr$ ratios. Blanks of Sr preparations were lower than 0.05 ng mL^{-1}.

Thirteen samples of dolostones constituting the host MVT mineralization were crushed and only dolomite crystals were powdered in an agate mortar and sieved in order to obtain their whole rock minor and

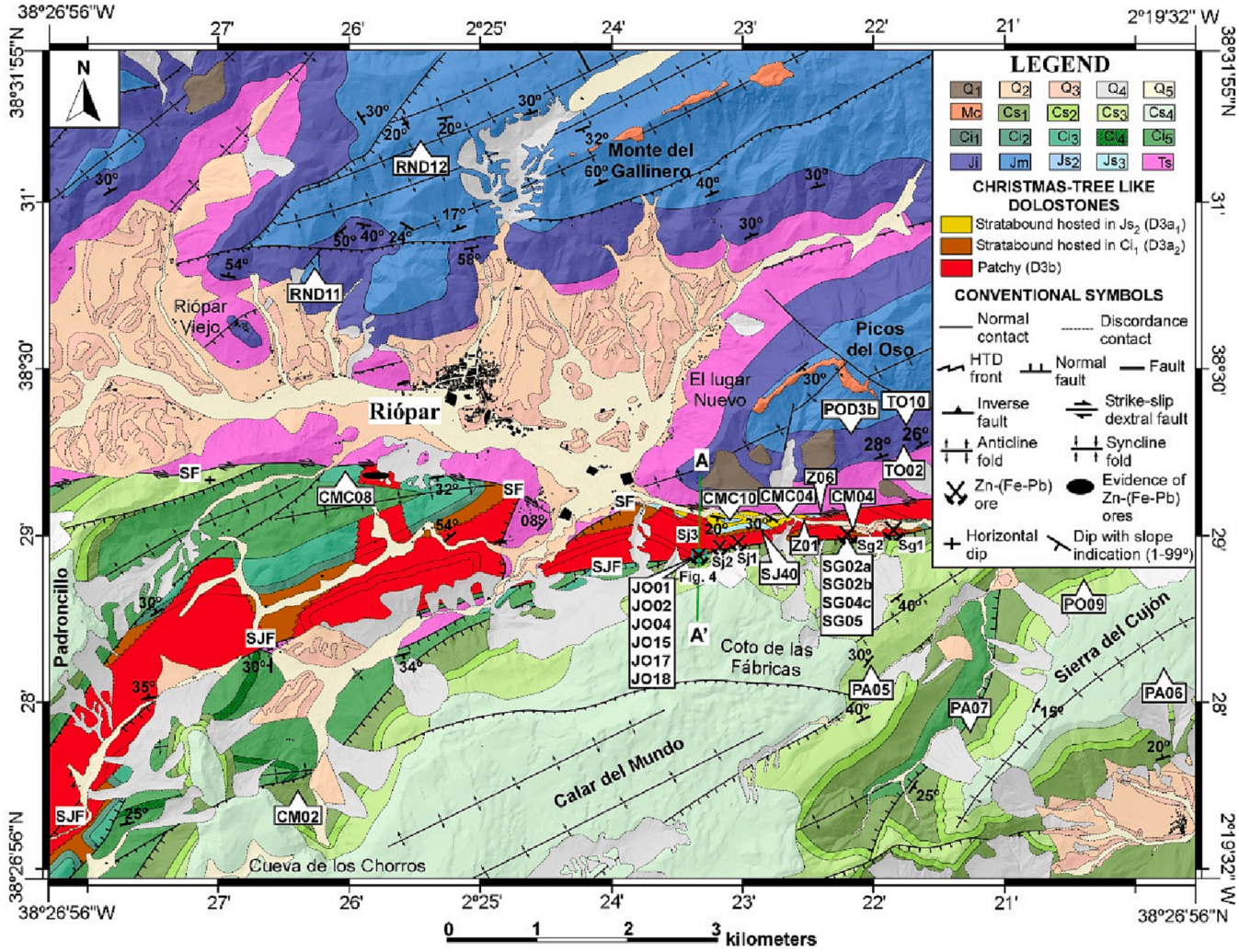

Fig. 3. Geological map of the Riópar area with the distribution and morphology of dolostones, the occurrence of Zn-(Fe-Pb) mineralization and sample location. Tr: Keuper Fm. (Triassic clays and sandstones); Ji: Carretas to Contreras-Madroño Fm. (Lower Jurassic D1 dolostones and limestones); Jm: Chorro Fm. (Middle Jurassic D2 dolostones); Js_2, Js_3, Ci_1: Sierra del Pozo Fm. (Kimmeridgian to Hauterivian limestones and marls); Ci_2: Cerro Lobo Fm. (Hauterivian to Valanginian marls and limestones); Ci_3: Arroyo de los Anchos Fm. (Barremian to Aptian pisolitic and "callouix noire" limestones); Ci_4: Utrillas facies (Aptian to Albian sandstones and clays with dolomitized limestone levels); Cs_1, Cs_2, Cs_3: Dolomítica Fm. (Cenomanian-Turonian D4 dolostones); Cs_4: Sierra de la Solana Fm. (Coniacian-Santonian limestones); Mc: Miocene polymictic conglomerate; Q_1: undifferentiated colluvium; Q_2: alluvial fans; Q_3: debris on alluvial funs; Q_4: recent colluvial; SF: Socovos fault; SJF: San Jorge fault; Sg1, Sg2: San Agustín ore deposits; Sj1, Sj2, Sj3: San Jorge ore deposits.

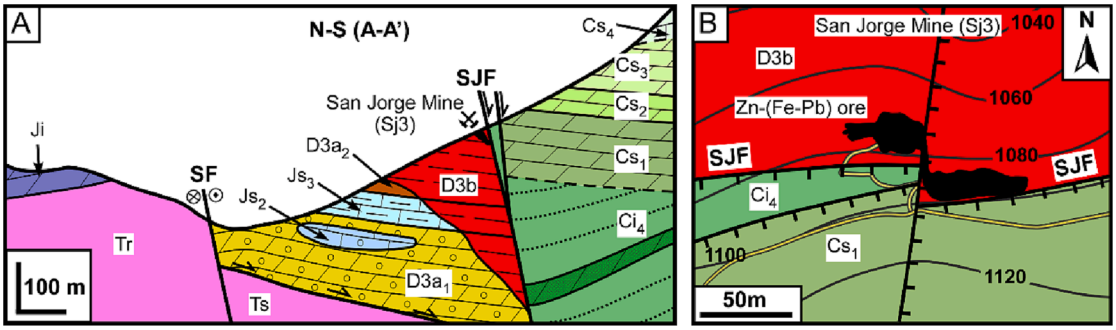

Fig. 4. Cross section (A) and detailed map (B) of the San Jorge Zn-(Fe-Pb) mineralized zone (Sj3). See Fig. 3 for location of cross section, detailed map, and legend. $D3a_1$: stratabound hydrothermal dolostone affecting Js_2 limestones (Lower Mb. of Sierra del Pozo Fm.); $D3a_2$: stratabound hydrothermal dolostone affecting Ci_1 limestones (Upper Mb. of Sierra del Pozo Fm.); D3b: patchy hydrothermal dolostone; SF: Socovos fault; SJF: San Jorge fault.

trace element composition. Minor and trace elements (including REE) of the samples were determined at ActLabs Laboratories, Ontario, Canada. Each sample was fused using a lithium metaborate-tetraborate mixture. The melt produced by this process was completely dissolved with 5% HNO_3. Zn, Y, La, Ce, Pr, Nd, Sm, Eu, Gd, Tb, Dy, Ho, Er, Tm, Yb, Lu, and Pb were analyzed by fusion-inductively mass spectrometer (FUS-MS).

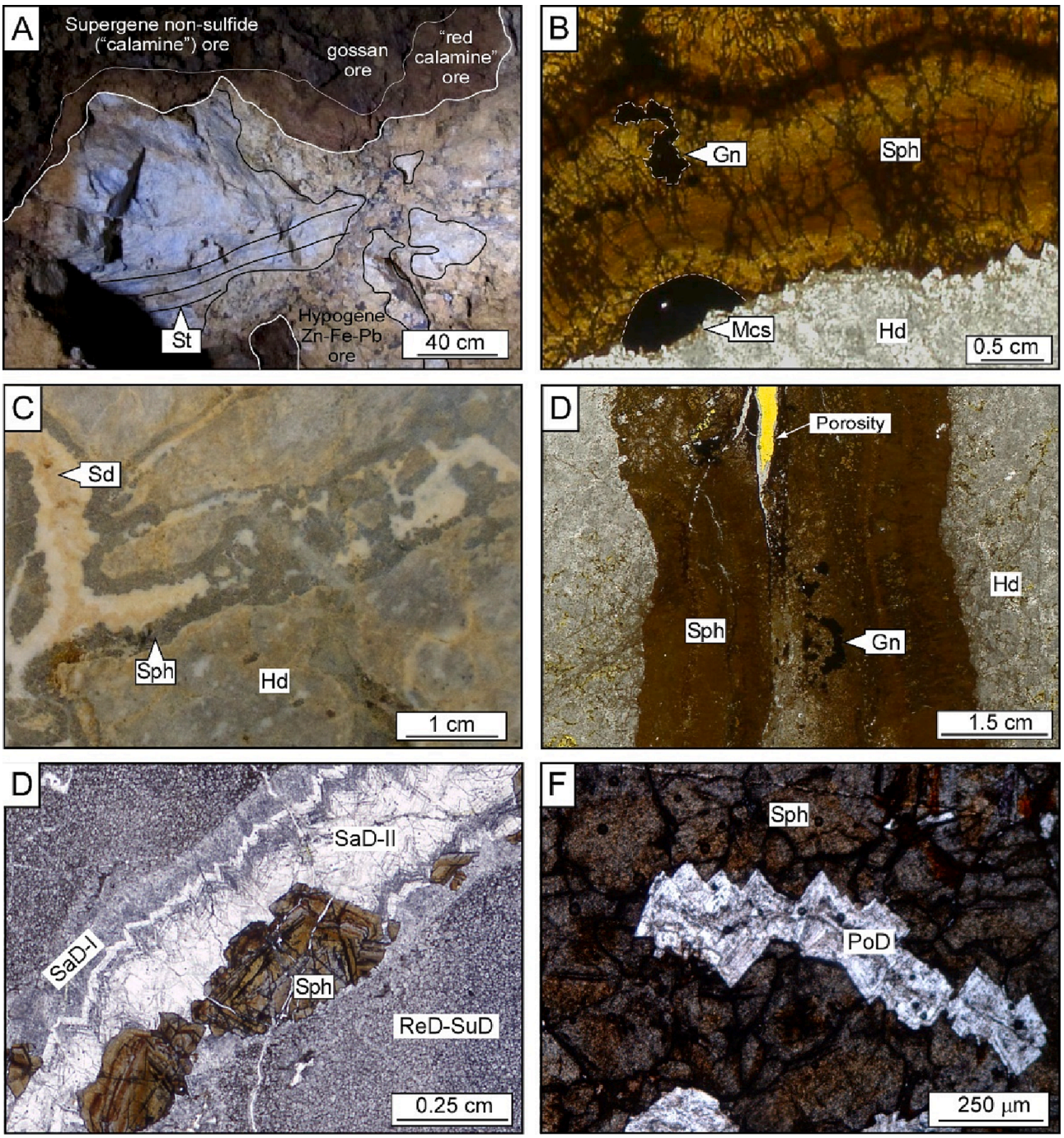

Fig. 5. A) Massive irregular hypogene and supergene Zn-(Fe-Pb) ore lenses hosted in partially stratified (St) dolostones (Hd). B) Transmitted light with parallel polarizer (TL-PP) microphotograph of sphalerite (Sph) vein with marcasite (Mcs) and galena (Gn) hosted in dolomite (Hd). C) Ore-cemented breccia hand sample. D) TL-PP microphotograph of sphalerite vein associated with porosity. E) TL-PP photomicrograph showing fracture filling by early non-planar saddle dolomite (SaD-I), sphalerite and late non-planar saddle dolomite (SaD-II) hosted in planar-s (subhedral) replacive to planar-e (euhedral) sucrosic dolomite transition (ReD-SuD). F) Porphyrotopic dolomite (PoD) replacing sphalerite crystals.

Detection limits for REE ranged from limits ranged from 0.02 to 0.05 mg kg^{-1}, whereas the rest of the elements ranged from 0.1 to 30 mg kg^{-1}. More information on the procedure, precision and accuracy of ACTLABS ICP-MS analyses can be found at https://www.actlabs.com.

1.4. Dolostone geobodies occurrences

In the Riópar area a large number of Mesozoic sedimentary units can be observed (Fig. 2). Triassic sandstones with clays and gypsum, and Lower to Middle Jurassic carbonates crop out in the northern block of the Socovos fault, whereas carbonates of Upper Cretaceous age appear in the southern block of the San Jorge fault. Upper Jurassic to Lower Cretaceous carbonates crop out between the two abovementioned tectonic structures. Furthermore, several dolomitized carbonates are also identified in the Riópar area (Fig. 3). Their distribution along the stratigraphic section are (Fig. 2): i) Lower Jurassic stratabound dolostones (D1); ii) Middle Jurassic stratabound dolostones (D2); iii) Upper Jurassic to Lower Cretaceous stratabound and patchy dolomitized carbonates (D3); and iv) Upper Cretaceous stratabound dolostones (D4).

Table 1
Carbon, oxygen and strontium isotope data from limestones (Lim), stratabound dolostones (St. Dol) and patchy dolomites (Pa. Dol), including descriptions of sample type, dolomite crystal types and mineralization types.

Sample-(analysis)	Formation	Rock type	Sampling type	Dolomite type	Relationship with mineralization	$\delta^{13}C$ (‰) VPDB	$\delta^{18}O$ (‰) VPDB	$\delta^{18}O$ (‰) VSMOW	$^{87}Sr/^{86}Sr$
TO02-(01)	Carretas	St. Dol.	Handpicked	Planar-e (replacive)	Unmineralized	+3.8	−1.9	+29.0	0.70749
TO02-(02)	Carretas	St. Dol.	Handpicked	Planar-s (replacive)	Unmineralized	+3.8	−1.9	+29.0	
TO10-(01)	Contreras-Madroño	Lim.	Whole rock			+2.6	−3.1	+27.7	0.70731
TO10-(02)	Contreras-Madraño	Lim.	Whole rock			+2.5	−3.2	+27.6	
POD3b-(01)	Contreras-Madroño	Lim.	Whole rock			+2.7	−2.6	+28.2	
RND11-(01)	Chorro	St. Dol.	Handpicked	Planar-e (sucrose)	Unmineralized	+3.2	−1.6	+29.3	0.70745
RND11-(02)	Chorro	St. Dol.	Handpicked	Planar-e (sucrose)	Unmineralized	+3.4	−1.1	+29.8	
RND12-(01)	Chorro	Lim.	Whole rock			+2.4	−2.8	+28.0	
RND12-(02)	Chorro	Lim.	Whole rock			+2.1	−3.0	+27.8	0.70737
CMC10-(01)	Lower Mb Sierra del Pozo	Lim.	Whole rock			+0.5	0.0	+30.9	
CMC04-(01)	Lower Mb Sierra del Pozo	St. Dol.	Handpicked	Planar-s (replacive)	Unmineralized	+0.4	−4.0	+26.7	0.70773
Z01-(01)	Lower Mb Sierra del Pozo	Pa. Dol.	Drilled	Planar-e (sucrose)	Unmineralized	+0.4	−4.1	+26.7	
Z01-(02)	Lower Mb Sierra del Pozo	Pa. Dol.	Drilled	Planar-e (sucrose)	Unmineralized	+0.5	−4.4	+26.4	
Z01-(03)	Lower Mb Sierra del Pozo	Pa. Dol.	Whole rock	Planar-e sucrose and non-planar saddle	Unmineralized	+0.6	−3.8	+27.0	0.70753
Z01-(04)	Lower Mb Sierra del Pozo	Pa. Dol.	Whole rock	Planar-e sucrose and non-planar saddle	Unmineralized	+0.8	−4.0	+26.8	0.70747
Z01-(05)	Lower Mb Sierra del Pozo	Pa. Dol.	Whole rock	Planar-e sucrose and non-planar saddle	Unmineralized	+0.9	−3.7	+27.1	0.70745
Z01-(06)	Lower Mb Sierra del Pozo	Pa. Dol.	Whole rock	Planar-e sucrose and non-planar saddle	Unmineralized	+0.8	−4.2	+26.6	0.70744
Z06-(01)	Middle Mb Sierra del Pozo	Lim.	Whole rock			+2.3	−3.0	+27.8	0.70723
Z06-(02)	Middle Mb Sierra del Pozo	Lim.	Whole rock			+2.3	−2.9	+27.9	
Z06-(03)	Middle Mb Sierra del Pozo	Lim.	Whole rock			+3.2	−3.0	+27.8	
Z06-(04)	Middle Mb Sierra del Pozo	Lim.	Whole rock			+3.0	−3.1	+27.7	
SG02a-(01)	Upper Mb Sierra del Pozo	St. Dol.	Whole rock	Planar-s and planar-e replacive)	Weakly mineralized (veinlets)	+0.1	−4.8	+26.0	0.70748
SG02a-(02)	Upper Mb Sierra del Pozo	St. Dol.	Drilled	Planar-e (replacive)	Weakly mineralized (veinlets)	0.0	−4.8	+26.0	
SG02b-(01)	Upper Mb Sierra del Pozo	St. Dol.	Drilled	Planar-e (replacive)	Weakly mineralized (dissemination)	+0.6	−4.4	+26.3	
SG02b-(02)	Upper Mb Sierra del Pozo	St. Dol.	Drilled	Planar-e (replacive)	Weakly mineralized (dissemination)	+0.4	−4.9	+25.9	
SG02b-(03)	Upper Mb Sierra del Pozo	St. Dol.	Drilled	Planar-s (replacive)	Weakly mineralized (dissemination)	+0.3	−4.7	+26.0	
SG05-(01)	Upper Mb Sierra del Pozo	St. Dol.	Whole rock	Planar-s and planar-e (replacive)	Weakly mineralized (dissemination)	+0.1	−3.8	+27.0	0.70773
CM04-(01)	Upper Mb Sierra del Pozo	St. Dol.	Drilled	Planar-s (replacive)	Weakly mineralized (veinlets)	+0.6	−4.0	+26.8	0.70743
CM04-(02)	Upper Mb Sierra del Pozo	St. Dol.	Drilled	Planar-e (replacive)	Host-rock of ore geobody lens	+0.4	−4.5	+26.3	
CM04-(03)	Upper Mb Sierra del Pozo	St. Dol.	Drilled	Planar-e (replacive)	Host-rock of ore geobody lens	+0.6	−3.9	+26.9	
CM04-(04)	Upper Mb Sierra del Pozo	St. Dol.	Drilled	Planar-s (replacive)	Host-rock of ore geobody lens	+0.6	−4.3	+26.5	
SJ40-(01)	Upper Mb Sierra del Pozo	St. Dol.	Whole rock	Planar-s and planar-e (replacive)	Host-rock of ore geobody lens	+0.1	−3.7	+27.1	0.70750
JO01-(01)	Upper Mb Sierra del Pozo	St. Dol.	Drilled	Planar-e (replacive)	Host-rock of ore geobody lens	+0.4	−5.3	+25.4	
JO01-(02)	Upper Mb Sierra del Pozo	St. Dol.	Drilled	Planar-s (replacive)	Host-rock of ore geobody lens	+0.2	−5.0	+25.8	
JO01-(03)	Upper Mb Sierra del Pozo	St. Dol.	Drilled	Planar-s (replacive)	Host-rock of ore geobody lens	+0.4	−5.3	+25.4	
SG02a-(02)	Upper Mb Sierra del Pozo	Pa. Dol.	Drilled	Non-planar (saddle)	Weakly mineralized (veinlets)	+0.1	−4.4	+26.4	
SG02a-(03)	Upper Mb Sierra del Pozo	Pa. Dol.	Drilled	Non-planar (saddle)	Weakly mineralized (veinlets)	−0.1	−4.8	+26.0	
SG02a-(04)	Upper Mb Sierra del Pozo	Pa. Dol.	Drilled	Non-planar (saddle)	Weakly mineralized (veinlets)	−0.1	−4.7	+26.1	
SG02a-(05)	Upper Mb Sierra del Pozo	Pa. Dol.	Drilled	Non-planar (saddle)	Weakly mineralized (veinlets)	−0.4	−4.3	+26.5	
SG02a-(06)	Upper Mb Sierra del Pozo	Pa. Dol.	Drilled	Non-planar (saddle)	Weakly mineralized (veinlets)	−0.1	−5.2	+25.6	

(*continued on next page*)

Table 1 (*continued*)

Sample-(analysis)	Formation	Rock type	Sampling type	Dolomite type	Relationship with mineralization	$\delta^{13}C$ (‰) VPDB	$\delta^{18}O$ (‰) VPDB	$\delta^{18}O$ (‰) VSMOW	$^{87}Sr/^{86}Sr$
SG02a-(07)	Upper Mb Sierra del Pozo	Pa. Dol.	Drilled	Non-planar (saddle)	Weakly mineralized (veinlets)	−0.3	−4.6	+26.1	
SG02a-(08)	Upper Mb Sierra del Pozo	Pa. Dol.	Drilled	Non-planar (saddle)	Weakly mineralized (veinlets)	−0.1	−4.3	+26.5	0.70799
SG02b-(04)	Upper Mb Sierra del Pozo	Pa. Dol.	Drilled	Non-planar (saddle)	Weakly mineralized (dissemination)	+0.4	−5.0	+25.8	
SG02b-(05)	Upper Mb Sierra del Pozo	Pa. Dol.	Drilled	Non-planar (saddle)	Weakly mineralized (dissemination)	+0.2	−4.8	+26.0	
SG02b-(06)	Upper Mb Sierra del Pozo	Pa. Dol.	Drilled	Non-planar (saddle)	Weakly mineralized (dissemination)	+0.4	−4.7	+26.0	
SG02b-(07)	Upper Mb Sierra del Pozo	Pa. Dol.	Whole rock	Non-planar (saddle)	Weakly mineralized (dissemination)	+0.5	−4.7	+26.1	
SG02b-(08)	Upper Mb Sierra del Pozo	Pa. Dol.	Drilled	Non-planar (saddle)	Weakly mineralized (dissemination)	+0.6	−4.4	+26.3	
SG02b-(09)	Upper Mb Sierra del Pozo	Pa. Dol.	Drilled	Non-planar (saddle)	Weakly mineralized (dissemination)	−0.2	−5.6	+25.2	
SG02b-(10)	Upper Mb Sierra del Pozo	Pa. Dol.	Drilled	Non-planar (saddle)	Weakly mineralized (dissemination)	0.0	−3.8	+27.0	
SG02b-(11)	Upper Mb Sierra del Pozo	Pa. Dol.	Drilled	Non-planar (saddle)	Weakly mineralized (dissemination)	+0.3	−4.6	+26.2	
SG02b-(12)	Upper Mb Sierra del Pozo	Pa. Dol.	Drilled	Non-planar (saddle)	Weakly mineralized (dissemination)	−0.2	−5.3	+25.4	
SG02b-(13)	Upper Mb Sierra del Pozo	Pa. Dol.	Drilled	Non-planar (saddle)	Weakly mineralized (dissemination)	+0.1	−4.2	+26.6	0.70766
SG02b-(14)	Upper Mb Sierra del Pozo	Pa. Dol.	Whole rock	Whole rock (non-planar saddle)	Weakly mineralized (dissemination)	+0.2	−4.8	+26.0	0.70803
SG04c-(01)	Upper Mb Sierra del Pozo	Pa. Dol.	Whole rock	Whole rock (non-planar saddle)	Weakly mineralized (veinlets)	−0.2	−4.2	+26.6	0.70782
SG05-(02)	Upper Mb Sierra del Pozo	Pa. Dol.	Whole rock	Whole rock (non-planar saddle)	Weakly mineralized (veinlets)	+0.2	−3.9	+26.9	0.70770
JO15-(01)	Upper Mb Sierra del Pozo	Pa. Dol.	Drilled	Planar-e (sucrose)	Host-rock of ore geobody lens	−0.6	−4.7	+26.0	
JO15-(02)	Upper Mb Sierra del Pozo	Pa. Dol.	Drilled	Planar-e (sucrose)	Host-rock of ore geobody lens	−0.6	−4.5	+26.3	
JO15-(03)	Upper Mb Sierra del Pozo	Pa. Dol.	Drilled	Planar-e (sucrose)	Host-rock of ore geobody lens	−0.7	−4.8	+25.9	
JO15-(04)	Upper Mb Sierra del Pozo	Pa. Dol.	Drilled	Planar-e (sucrose)	Host-rock of ore geobody lens	−0.7	−4.8	+26.0	
JO15-(05)	Upper Mb Sierra del Pozo	Pa. Dol.	Drilled	Planar-e (sucrose)	Host-rock of ore geobody lens	−0.5	−4.8	+26.0	
JO15-(06)	Upper Mb Sierra del Pozo	Pa. Dol.	Drilled	Planar-e (sucrose)	Host-rock of ore geobody lens	−0.5	−4.7	+26.0	
JO15-(07)	Upper Mb Sierra del Pozo	Pa. Dol.	Drilled	Planar-e (sucrose)	Host-rock of ore geobody lens	−0.6	−4.8	+25.9	
JO15-(08)	Upper Mb Sierra del Pozo	Pa. Dol.	Drilled	Planar-e (sucrose)	Host-rock of ore geobody lens	−0.6	−4.7	+26.0	0.70745
JO16-(01)	Upper Mb Sierra del Pozo	Pa. Dol.	Drilled	Planar-e (sucrose)	Host-rock of ore geobody lens	−0.2	−4.9	+25.9	
JO16-(02)	Upper Mb Sierra del Pozo	Pa. Dol.	Drilled	Planar-e (sucrose)	Host-rock of ore geobody lens	−0.1	−4.9	+25.9	
JO16-(03)	Upper Mb Sierra del Pozo	Pa. Dol.	Drilled	Planar-e (sucrose)	Host-rock of ore geobody lens	−0.2	−4.7	+26.0	
JO16-(04)	Upper Mb Sierra del Pozo	Pa. Dol.	Drilled	Planar-e (sucrose)	Host-rock of ore geobody lens	−2.0	−4.9	+25.9	
JO17-(01)	Upper Mb Sierra del Pozo	Pa. Dol.	Drilled	Planar-e (sucrose)	Host-rock of ore geobody lens	−0.3	−5.1	+25.6	
JO17-(02)	Upper Mb Sierra del Pozo	Pa. Dol.	Drilled	Planar-e (sucrose)	Host-rock of ore geobody lens	−0.4	−5.5	+25.2	
JO17-(03)	Upper Mb Sierra del Pozo	Pa. Dol.	Drilled	Planar-e (sucrose)	Host-rock of ore geobody lens	−0.4	−5.6	+25.2	
JO17-(04)	Upper Mb Sierra del Pozo	Pa. Dol.	Drilled	Planar-e (sucrose)	Host-rock of ore geobody lens	−0.2	−5.2	+25.6	
JO17-(05)	Upper Mb Sierra del Pozo	Pa. Dol.	Drilled	Planar-e (sucrose)	Host-rock of ore geobody lens	−0.3	−5.3	+25.4	
JO17-(06)	Upper Mb Sierra del Pozo	Pa. Dol.	Drilled	Planar-e (sucrose)	Host-rock of ore geobody lens	−0.7	−5.6	+25.2	
JO17-(07)	Upper Mb Sierra del Pozo	Pa. Dol.	Drilled	Planar-e (sucrose)	Host-rock of ore geobody lens	−0.2	−5.1	+25.7	0.70738
JO18-(01)	Upper Mb Sierra del Pozo	Pa. Dol.	Drilled	Planar-e (sucrose)	Host-rock of ore geobody lens	−0.4	−5.4	+25.4	0.70739
JO02-(01)	Upper Mb Sierra del Pozo	Pa. Dol.	Drilled	Planar-e (sucrose)	Host-rock of ore geobody lens	−0.4	−5.5	+25.2	
JO02-(02)	Upper Mb Sierra del Pozo	Pa. Dol.	Drilled	Planar-e (sucrose)	Host-rock of ore geobody lens	−0.5	−5.6	+25.1	

(*continued on next page*)

Table 1 (*continued*)

Sample-(analysis)	Formation	Rock type	Sampling type	Dolomite type	Relationship with mineralization	δ ^{13}C (‰) VPDB	δ^{18}O (‰) VPDB	δ^{18}O (‰) VSMOW	^{87}Sr/^{86}Sr
JO02-(03)	Upper Mb Sierra del Pozo	Pa. Dol.	Drilled	Planar-e (sucrose)	Host-rock of ore geobody lens	−0.4	−5.7	+25.1	
JO02-(04)	Upper Mb Sierra del Pozo	Pa. Dol.	Drilled	Planar-e (sucrose)	Host-rock of ore geobody lens	−0.3	−5.6	+25.1	
JO02-(05)	Upper Mb Sierra del Pozo	Pa. Dol.	Drilled	Planar-e (sucrose)	Host-rock of ore geobody lens	−0.6	−5.6	+25.1	
JO02-(06)	Upper Mb Sierra del Pozo	Pa. Dol.	Drilled	Planar-e (sucrose)	Host-rock of ore geobody lens	−0.4	−5.2	+25.1	0.70736
JO01-(04)	Upper Mb Sierra del Pozo	Pa. Dol.	Drilled	Planar-e (sucrose)	Host-rock of ore geobody lens	+0.4	−5.1	+25.6	
JO01-(05)	Upper Mb Sierra del Pozo	Pa. Dol.	Drilled	Planar-e (sucrose)	Host-rock of ore geobody lens	+0.4	−5.4	+25.4	
JO01-(06)	Upper Mb Sierra del Pozo	Pa. Dol.	Drilled	Planar-e (sucrose)	Host-rock of ore geobody lens	+0.4	−5.0	+25.8	
JO01-(07)	Upper Mb Sierra del Pozo	Pa. Dol.	Whole rock	Planar-e sucrose and non-planar saddle	Host-rock of ore geobody lens	+0.3	−4.7	+26.1	0.70830
JO01-(08)	Upper Mb Sierra del Pozo	Pa. Dol.	Whole rock	Planar-e sucrose and non-planar saddle	Host-rock of ore geobody lens	0.0	−4.2	+26.6	
JO01-(09)	Upper Mb Sierra del Pozo	Pa. Dol.	Drilled	Non-planar (saddle)	Host-rock of ore geobody lens	0.0	−4.1	+26.7	
JO01-(10)	Upper Mb Sierra del Pozo	Pa. Dol.	Drilled	Non-planar (saddle)	Host-rock of ore geobody lens	+0.1	−4.3	+26.5	0.70830
JO04-(01)	Upper Mb Sierra del Pozo	Pa. Dol.	Drilled	Planar-e (sucrose)	Host-rock of ore geobody lens	−0.4	−4.8	+26.0	
JO04-(02)	Upper Mb Sierra del Pozo	Pa. Dol.	Drilled	Planar-e (sucrose)	Host-rock of ore geobody lens	−0.5	−4.7	+26.1	
JO04-(03)	Upper Mb Sierra del Pozo	Pa. Dol.	Drilled	Planar-e (sucrose)	Host-rock of ore geobody lens	−0.1	−4.7	+26.1	
JO04-(04)	Upper Mb Sierra del Pozo	Pa. Dol.	Drilled	Planar-e (sucrose)	Host-rock of ore geobody lens	−2.3	−4.4	+26.4	
CMC08-(01)	Lower Mb Arroyo de los Anchos	Lim.	Whole rock			+2.8	−3.2	+27.6	
CM02-(01)	Lower Mb Dolomitica	St. Dol.	Handpicked	Planar-e (replacive)	Unmineralized	+2.7	−1.3	+29.5	0.70764
CM02-(02)	Lower Mb Dolomitica	St. Dol.	Handpicked	Planar-s (replacive)	Unmineralized	+2.6	−1.7	+29.2	
PA07-(01)	Lower Mb Dolomitica	St. Dol.	Handpicked	Planar-s (replacive)	Unmineralized	+2.5	−3.2	+27.6	
PA07-(02)	Lower Mb Dolomitica	St. Dol.	Handpicked	Planar-e (replacive)	Unmineralized	+2.5	−3.2	+27.6	
PO09-(01)	Middle Mb Dolomitica	St. Dol.	Handpicked	Planar-e (replacive)	Unmineralized	+2.6	−3.1	+27.7	0.70746
PA05-(01)	Upper Mb Dolomitica	St. Dol.	Handpicked	Planar-e (replacive)	Unmineralized	+2.1	−2.4	+28.4	0.70736
PA06-(01)	Sierra de la Solana	Lim.	Whole rock			+3.0	−2.2	+28.7	0.70746
PA06-(02)	Sierra de la Solana	Lim.	Whole rock			+2.8	−1.3	+29.6	

1.5. Lower Jurassic stratabound dolostones (D1)

The Lower Jurassic stratabound dolostones (D1) are part of the Carretas Fm., and the Contreras-Madroño Fm. (Hettangian-Pleinsbachian; Figs. 2 and 3), and characterized by a reddish to grayish color (Fig. 6a). In the Riópar area, the D1 stratabound dolostone thickness exceeds 150 m. It is constituted by two types of replacive dolomite crystals (Fig. 6b): i) dolomites with anhedral to subhedral morphologies of sizes less than 100 μm (planar-s); and ii) zoned rhombohedral euhedral dolomites smaller than 1.5 mm (planar-e). Although these dolostones do not commonly present a well-developed porosity, some samples display isolated intercrystalline pores with diameters of less than 0.5 mm (Fig. 6b). The dolomitization is mainly fabric-retentive, as oolitic allochems and porosity of the precursor limestones are recognized, preserving the original depositional fabrics (i.e., stratification). At the top of the dolomitization front (Fig. 6a), non-dolomitized fossiliferous intra-pelsparitic and intra-oosparitic grainstones to packstones, and intra-pelmicritic wackstones to mudstones of the Contreras-Madroño Fm. occur (Fig. 6d). The dolomitization front is observed mainly along stylolites and millimeter-size fractures (Fig. 6c). The lithological components recognized in the Contreras-Madroño Fm. limestones included gastropods, bivalves, foraminifera (genus: *Ammomarginulina*; *Verneuilinoides*, *Textularia*, *Redmondina*, *Spirillina*, *Lenticulina*, *Triloculina*, *Quinqueloculina* and *Epistomina*), dasycladaceae green algae and sponge spicules (Fig. 6d).

1.6. Middle Jurassic stratabound dolostones (D2)

The Middle Jurassic stratabound dolomitized limestones, which are located within the Chorro carbonate Fm. (Aalenian-Callovian: Figs. 2 and 3), are characterized by a whiteish color developed in greater than 250 m of the sedimentary sequence (Fig. 7a). D2 dolostones are constituted by fine to coarse planar-e sucrosic dolomite crystals with less than 1 mm in size (Fig. 7b) with common intercrystalline millimetric to centimetric pores. Occasionally, this porosity reaches 10% of the volume (Fig. 7b). The replacement is fabric-retentive as oolitic ghosts can be identified, although original sedimentary structures, such as stratification, are rarely preserved. At the top of the D2 stratabound dolostone, non-dolomitized fossiliferous intra-oosparitic grainstones to packstones, and to a lesser extend mudstones, occur mainly along a penetrative dolomitization front that is parallel to stratification, as well as along stylolites and millimeter-size fractures. The main recognized macrofauna of upper limestones included gastropods, bivalves (predominantly ostreids), corals, sponge spicules and echinoids (Fig. 7c and d). Usually, the ooids, with supported grain and concentric and elongated morphologies, are micritized (bahmitic peloids: Fig. 7c).

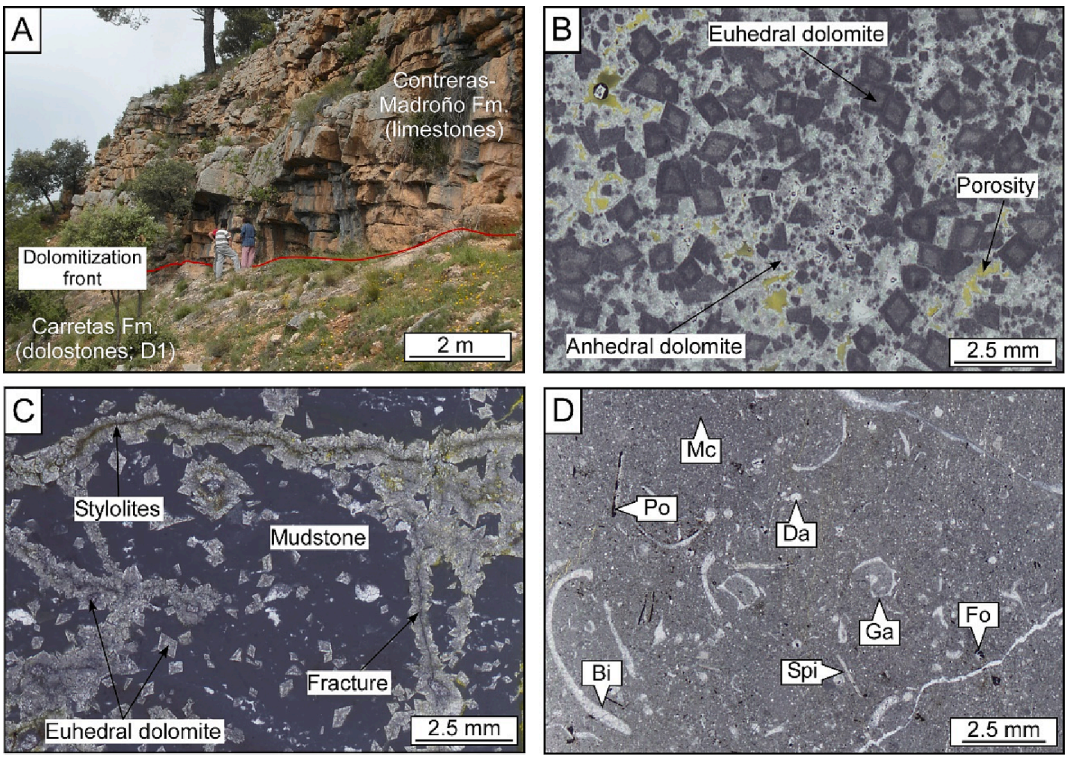

Fig. 6. Characteristics of the Lower Jurassic stratabound dolostones (D1: Carretas Fm.). A) Photograph of the dolomitization front that delimits the Carretas Fm. dolostones (bottom) and the Contreras-Madroño Fm. limestones (top). B) Transmitted light with parallel polarizer (TL-PP) microphotograph of the D1 dolostones. C) TL-PP microphotograph of the dolomitization front. In this case, the dolomitization affects mudstones of the Contreras-Madroño Fm. D) Petrographic characteristic of a representative intra-pelmicritic wackstone of the Contreras-Madroño Fm. (TL-PP). Bi: bivalve; Da: dasicladaceae green algae; Fo: foraminifera; Ga: gastropod; Mc: microcrystalline matrix of calcite; Po: oxidized pyrite; Spi: sponge spicule; St: stylolite.

Upper Jurassic to Lower Cretaceous stratabound and patchy dolomitized carbonates (D3).

Two types of dolostone geobodies have been identified in the Upper Jurassic to Lower Cretaceous carbonate succession (Fig. 2; Navarro-Ciurana et al., 2016a): one characterized by grey to brown color and stratabound morphology (D3a), which evolves into a second type of white patchy dolostone (D3b) (Fig. 8a). The resulting dolostone morphology may be conceived as a Christmas-tree like morphology (Fig. 4), with stratabound branches joined by patchy vertical trunks (Fig. 8a). These types of dolostones crop out over an area of 4.6 km^2 between San Jorge and Socovos faults (Fig. 3).

Two D3a stratabound dolostones preserving the original depositional fabrics (e.g., stratification, lamination) were observed in the Lower and the Upper Mb. of Sierra del Pozo Fm. intra-oosparitic grainstones to packstones and mudstones (Figs. 2 and 3). They are constituted by microcrystalline planar-s to planar-e replacive dolomite crystals (Fig. 8b and c). The Lower Mb. of Sierra del Pozo Fm. is partially dolomitized ($D3a_1$) as it preserves oolitic limestone lenses, which are constituted by grainstones, oosparitic packstones and mudstones (Fig. 8d). Also, this stratabound dolostone type contains oolitic moldic porosity and oolitic ghosts (Fig. 8b and c). On the other hand, the Upper Mb. has been completely dolomitized ($D3a_2$), extensively replacing intra-oosparitic grainstones and packstones, and occasionally with abundant orbitolinid moldic porosity, but preserving the stratification (Fig. 8e). The stratabound dolomitization fronts are locally wavy but commonly follow the bedding (Fig. 8f). The Middle Mb. of the Sierra del Pozo Fm. (nodular gray limestones and highly stylolithized marly limestones) is not affected by stratabound dolomitization and shows an incipient dolomitization across stylolites and bedding (Fig. 8g).

Different D3b patchy dolostones have been identified affecting the Lower Mb. of the Sierra del Pozo to the Arroyo de los Anchos Fms. (Figs. 2 and 3). The latter is easily recognized in the field by the abundant black pebbles (Fig. 9c). As both formations are hosted in the same Upper Jurassic to Lower Cretaceous carbonate sequence, the different patches can be considered as parts of a single dolostone body. They are constituted by planar-e sucrosic dolomite crystals and fine to coarse non-planar saddle dolomites, with highly developed porosity (Fig. 9a). Besides the larger bodies, saddle dolomite is also found forming rhythmic ('zebra') textures (Fig. 9b), cementing breccias around small fractures (Fig. 9c) and along stratification surfaces within the stratabound dolostones (Fig. 9d). The patchy dolomitized bodies gradually fuse with the two stratabound dolostone units ($D3a_1$ and $D3a_2$), commonly obliterating the sedimentary fabrics (Fig. 8a). Nevertheless, the contact front with the undolomitized carbonates is sharp, cross-cutting bedding and stratification and occur cementing fractures. Moreover, patchy dolostone crop out closer to the WE-trending and S-dipping San Jorge fault rather than the NW-trending Socovos dextral strike-slip fault (Figs. 3 and 4), suggesting a structural control for these geobodies. Dolomitization is more pervasive near the San Jorge fault, where the processes of replacement of carbonate units by dolomites are highly penetrative, completely obliterating sedimentary structures such as stratification and laminations (Fig. 9d). Traditionally, these dolomites were assigned to Middle Jurassic age (e.g., Fernández-Gianotti et al., 2001), probably due to their similar appearance with the D2 dolostones. Nevertheless, the presence of orbitolinid moldic porosity (Fig. 9e) and the stratigraphic correlation with nearby lithostratigraphic units, confirm that the undolomitized carbonates were deposited during the Upper Jurassic - Lower Cretaceous. Additionally, the Upper Mb. of Sierra del Pozo Fm. D3 dolostones constitute the host rocks of the Riópar MVT Zn-(Fe-Pb) deposit, and associated supergene ores (see Navarro-Ciurana et al., 2016b, 2017).

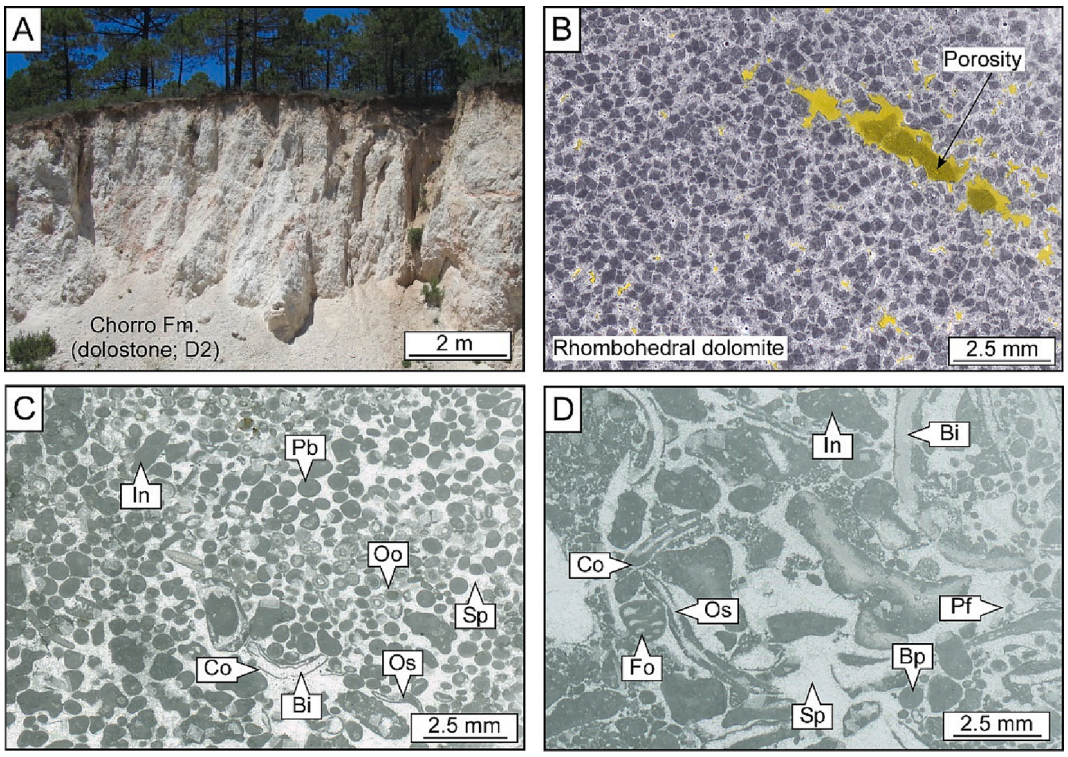

Fig. 7. Characteristics of the Middle Jurassic stratabound dolostones (D2: Chorro Fm.). A) Outcrop photograph of the D2 dolostones. B) TL-PP microphotograph of the D2 dolostones showing fine to coarse planar-e sucrosic dolomite crystals and pronounced intercrystalline porosity. C) TL-PP microphotograph of a non-dolomitized intra-oosparitic grainstone sample of the Chorro Fm. D) TL-PP microphotograph of a non-dolomitized intrapelmicritic packstone of the Chorro Fm. Bi: bivalve; Co: cortoid (micritic envelope); In: intraclast; Fo: foraminifera; Oo: oolith; Os: ostreido; Pb: bahmitic peloid (micritized ooid); Pf: fecal peloid (pellet); Sp: sparite.

1.7. Upper Cretaceous stratabound dolostones (D4)

The Upper Cretaceous sedimentary sequence (around 600 m thick) is represented by the Dolomítica and the Sierra de la Solana Fms. (D4: Figs. 2 and 3). The Upper Cretaceous stratabound dolomitized Cenomanian to Turonian limestones (Fig. 10a) are formed by fine planar-s to planar-e dolomite crystals (Fig. 10b and c). They are characterized by three different members: i) the Lower Mb. (D4a; Lower Cenomanian), which is constituted by ochre microcrystalline dolostones with orbitolinid ghosts; ii) the Middle Mb. (D4b; Upper Cenomanian), formed by white dolostones with oolitic ghosts and interbedded thin dolomitic marls; and iii) the Upper Mb. (D4c: Turonian), which is constituted by grey massive dolostones.

The D4a dolostones, which appears discordantly over the Utrillas Fm., are constituted by anhedral to subhedral dolomite crystals of less than 200 μm (Fig. 10b). In addition, these dolostones show a certain content of detrital quartz (Fig. 10b), suggesting a continental influence during the formation of the precursor limestone. On the other hand, fossil 'ghosts' (contours) and intraclasts have been observed (Fig. 10b), indicating that these dolostones were formed by the replacement of a pre-existing limestone. Petrographically, the D4b and D4c dolostones do not show substantial differences. These two dolostone units are characterized by the absence of detrital components and by the presence of fossil molds ('ghosts'), mainly orbitolinids (Fig. 10c). Two dolomite types have been recognized (Fig. 10c): i) anhedral to subhedral (planar-s replacive) dark dolomite crystals with less than 50 μm in size; and ii) euhedral (planar-e replacive) whitish dolomite crystals with less than 100 μm in size that replace fossil remnants. The D4 dolostone unit is discordantly overlaid by whitish limestones of the Sierra de la Solana Fm. (Fig. 10a), which are constituted by bioplemicritic and biointramicritic wackstones and packstones with gastropods, rudists, corals and echinoderm spicules (Fig. 10d).

1.8. Carbon, oxygen and strontium isotope characterization

The $\delta^{13}C_{VPDB}$, $\delta^{18}O_{VSMOW}$ and $^{87}Sr/^{86}Sr$ analytical results of Jurassic to Cretaceous limestone and dolostone (D1, D2, D3 and D4) samples are shown in Table 1. All limestones from Lower Jurassic to Upper Cretaceous (Fig. 11) show a narrow range of $\delta^{13}C_{VPDB}$ and $\delta^{18}O_{VSMOW}$ values between +0.5 to +3.2‰ and from +27.6 to +30.9‰, respectively (Table 1). Furthermore, the analyzed limestones exhibit $^{87}Sr/^{86}Sr$ ratios of 0.70723 to 0.70746 (Table 1). These values are compatible with carbonates precipitated from Jurassic to Cretaceous seawater (Veizer et al., 1999; Figs. 12 and 13).

D1 and D2 stratabound dolostones (Fig. 11) have $\delta^{13}C_{VPDB}$ values ranging from +3.2 to +3.8‰, $\delta^{18}O_{VSMOW}$ from +29.0 to +29.8‰ and $^{87}Sr/^{86}Sr$ ratios from 0.70745 to 0.70749 (Table 1). On the other hand, the isotopic signature of D4 stratabound dolostones (Fig. 11) ranges from +2.1 to +2.7‰ for $\delta^{13}C_{VPDB}$, from +27.6 to +29.5‰ for $\delta^{18}O_{VSMOW}$, and from 0.70736 to 0.70764 for $^{87}Sr/^{86}Sr$ (Table 1). Similar to marine limestones, these stratabound dolostone geobodies are close to the reported Jurassic to Cretaceous seawater values (Veizer et al., 1999); Figs. 12 and 13).

The D3a stratabound dolostones (Fig. 11) have $\delta^{13}C_{VPDB}$ values from +0.0 to +0.6‰, $\delta^{18}O_{VSMOW}$ from +25.4 to +27.0‰ and $^{87}Sr/^{86}Sr$ ratios from 0.70743 to 0.70773 (Figs. 12 and 13). Carbon and oxygen isotope values of this type of D3a stratabound dolostones are lower (Figs. 11 and 12), and $^{87}Sr/^{86}Sr$ signature generally higher (Figs. 11 and 13), than the D1, D2 and D4 stratabound dolostones, suggesting a different origin than the carbonates precipitated from Jurassic to Cretaceous seawater.

The D3b patchy dolostones show similar C and O isotope values ($\delta^{13}C_{VPDB}$: −2.3 to +0.9‰; $\delta^{18}O_{VSMOW}$: +25.1 to +27.1‰) than the D3a stratabound dolostones (Fig. 11), although D3a shows more restricted $\delta^{13}C$ values than the D3b (Fig. 12). Furthermore, D3b patchy dolostones have $^{87}Sr/^{86}Sr$ values of 0.70736 to 0.70830, mostly higher than D3a

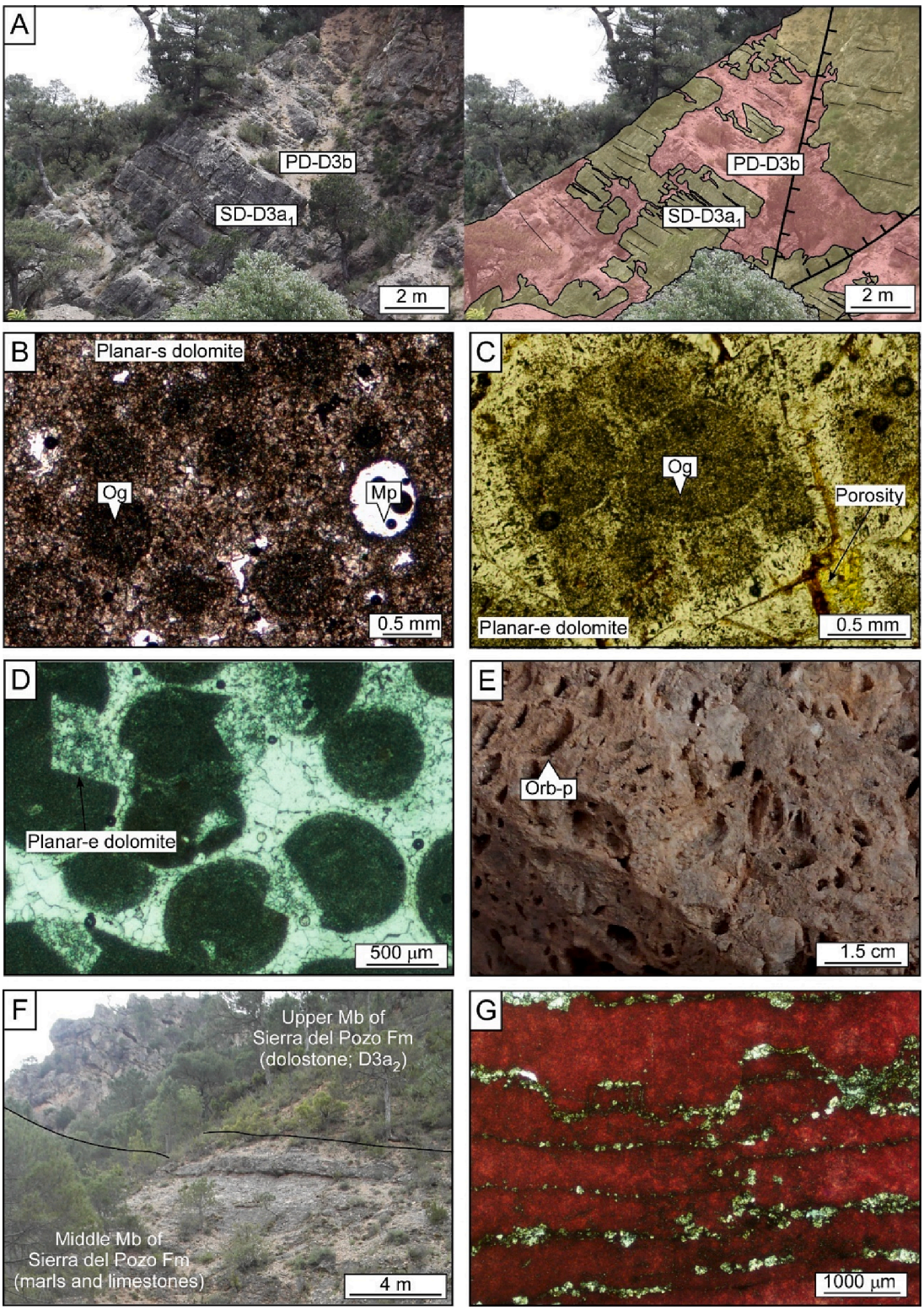

Fig. 8. Characteristics of the Upper Jurassic to Lower Cretaceous stratabound (D3a) dolomitized carbonates. A) Fine microcrystalline $D3a_1$ stratabound dolostone (SD-$D3a_1$: grey to brown color) of the Lower Mb. of the Sierra del Pozo Fm., preserving the original stratification and associated with D3b patchy dolostones (PD-D3b: whitish to greyish color), which are fabric destructive. B) Transmitted light with parallel polarizer (TL-PP) microphotograph of planar-s dolomite from D3a dolostone, oolitic ghosts (Og) and moldic porosity (Mp) derived from dissolution of ooids. C) TL-PP photomicrograph of planar-e dolomite from $D3a_1$ dolostone showing cloudy centers and light borders with intercrystalline porosity (yellow color). D) TL-PP photomicrograph of oolitic limestone lenses from the Lower Mb. of the Sierra del Pozo Fm. E) Orbitolinid moldic porosity (Orb-p) from the $D3a_2$ Upper Mb. of the Sierra del Pozo D3a stratabound dolostone. F) Contact between the Middle and the Upper Mbs. of the Sierra del Pozo Fm. constituted by limestones and marls, and dolostones ($D3a_2$), respectively. G) TL-PP photomicrograph of stylolithized marly limestones from Middle Mb. of Sierra del Pozo Fm., with planar-e dolomites along stylolites (red color is calcite stained by K-ferricyanide).

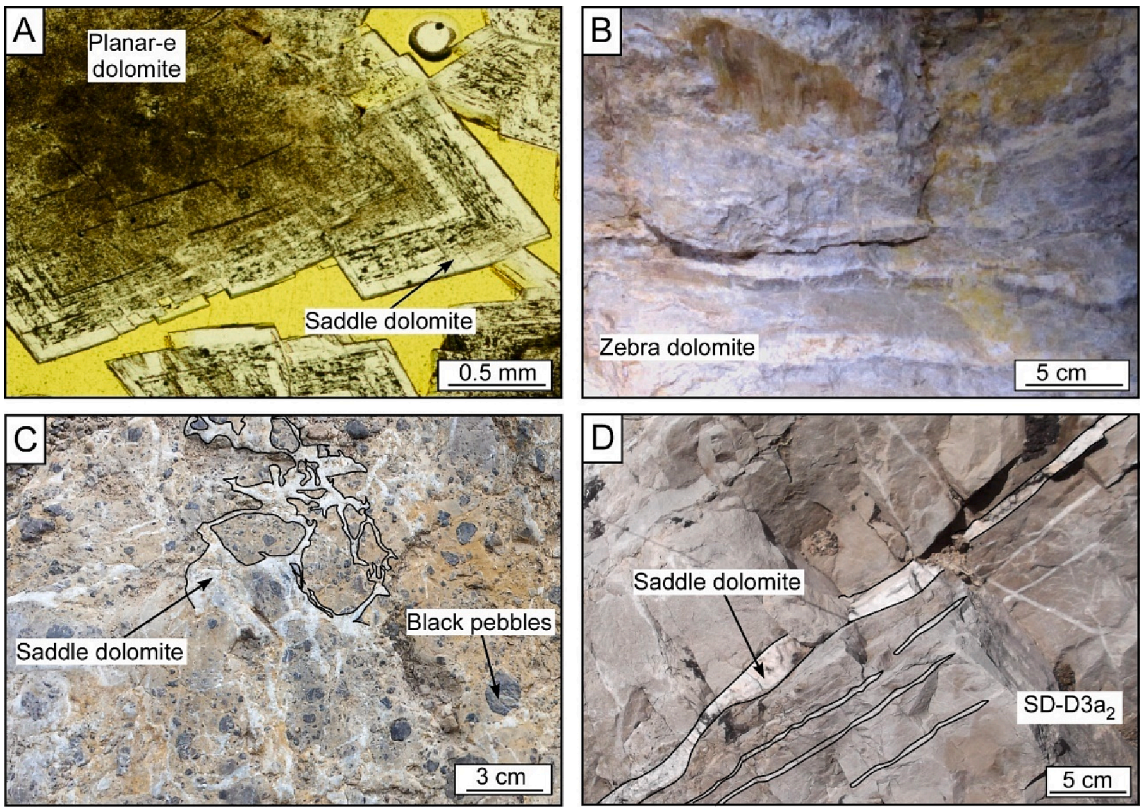

Fig. 9. Characteristics of Upper Jurassic to Lower Cretaceous patchy dolostones (D3b). A) Transmitted light with parallel polarizer (TL-PP) microphotograph of saddle dolomite showing cloudy centers that consists of planar-e crystals with well-developed intercrystalline porosity (Ip: yellow zones). B) Hand specimen of D3b patchy dolostone with rhythmic or zebra-like dolomite texture. C) Limestone with black pebbles ("cailloux noire") from the Lower Mb. of the Arroyo de los Anchos Fm. with saddle dolomite cementing breccias around small fractures. D) Saddle dolomite along stratigraphic planes of $D3a_2$ stratabound dolostone (SD-$D3a_1$) from the Upper Mb. of the Sierra del Pozo Fm.

stratabound dolostones (Fig. 13). On the other hand, the $D3a_2$ stratabound and D3b patchy dolostones hosting Zn-(Fe-Pb) mineralization (fertile dolostones: Upper Mb. of the Sierra del Pozo Fm.; Fig. 11) have a wider range of C, O and Sr isotope values ($\delta^{13}C_{VPDB}$: −2.3 to +0.6‰; $\delta^{18}O_{VSMOW}$: +25.1 to +27.0‰; $^{87}Sr/^{86}Sr$: 0.70736 to 0.70830: Fig. 12a and 13a) than $D3a_1$ stratabound and D3b patchy barren dolostones hosted in the Lower Mb. of the Sierra del Pozo Fm. ($\delta^{13}C_{VPDB}$: +0.4 to +0.9‰; $\delta^{18}O_{VSMOW}$: +26.4 to +27.1‰; $^{87}Sr/^{86}Sr$: 0.70774 to 0.70753: Figs. 11, 12b and 13b).

1.9. REE geochemistry

Rare Earth Element (REE) concentrations were analyzed in D3 stratabound and patchy HTDs, with the objective to search geochemical differences between mineralized (fertile) and barren dolostones. REE contents of the studied dolomites are summarized in Table 2.

The analyzed dolomite samples exhibit highly variable REE contents, with ∑REE in the range of 4.56 to 53.79 mg kg^{-1} (avg. = 19.15 mg kg^{-1}). REE contents of D3 stratabound and patchy dolostones are comparable with those studied in similar rocks in other localities, such as China (Wang et al., 2014; Li et al., 2016; Huang et al., 2022; Xuefeng et al., 2008; Chang et al., 2020), Italy (Hou et al., 2016), Canada (Tortola et al., 2020; Azomani et al., 2013), among others. Light REE (LREE), from lanthanum to europium, are enriched (∑LREE = 4.08–46.76 mg kg^{-1}, avg. = 17.24 mg kg^{-1}) compared to heavy REEs (HREE), from gadolinium to lutetium (∑HREE = 0.48–7.03 mg kg^{-1}, avg. = 1.92 mg kg^{-1}; Table 2). The LREE/HREE ratios of hydrothermal dolostones vary from 6.65 to 25.85 (avg. = 10.68; Table 2). The lowest total REE concentrations are found in the barren patchy dolostones (4.56 to 7.38 mg kg^{-1}, avg. = 6.15 mg kg^{-1}), whereas the highest REE contents are found in mineralized patchy (∑HREE = 14.10 – 29.69 mg kg^{-1}, avg. = 20.20 mg kg^{-1}) and stratabound dolostones (∑HREE = 14.36 – 53.79 mg kg^{-1}, avg. = 34.39 mg kg^{-1}). This geochemical differentiation is also reflected in Pb and Zn contents (Table 2): barren dolomites contain the lowest Zn and Pb concentrations whereas weakly and highly mineralized dolostones (HTDs hosting to ore body lenses; Table 1) show the highest Zn and Pb content.

The chondrite-normalized (CN) REE plot (Fig. 14) reveals broadly similar distribution patterns for all samples, with negative slopes for LREE and fairly horizontal HREE segments. This geometry results from the relative enrichment of LREE to Middle REE ($3.03 \leq La_{CN}/Sm_{CN} \leq 7.55$) and HREE ($7.88 \leq La_{CN}/Yb_{CN} \leq 48.94$), and of Middle REE to HREE ($1.84 \leq Sm_{CN}/Yb_{CN} \leq 12.12$; Table 2). $(Ce/Ce^*)c_N$ values of 0.61 to 0.84 and $(Eu/Eu^*)c_N$ values of 0.66 to 0.89 indicate a negative Ce and Eu anomalies (Table 2 and Fig. 14). Furthermore, D3 stratabound and patchy hydrothermal dolomite geobodies are characterized by a MREE bulge in the Post Archean Australian Shale-normalized (PAASN) REE plot (Fig. 15). The $(Ce/Ce^*)_{PAASN}$ ratio ranges from 0.64 to 0.97, $(Pr/Pr^*)_{PAASN}$ varies between 0.96 and 1.11, and $(Eu/Eu^*)_{PAASN}$ falls between 1.04 and 1.46 (Table 2). Unlike to chondrite normalization, REE values normalized to PAAS differentiate a positive Eu and a negative Ce anomaly of dolomites, and in consequence discriminate with more precision the character of the dolomitizing fluids (e.g., Piper and Bau, 2013).

2. Discussion

2.1. Origin of dolomite geobodies: marine vs hydrothermal

Sparse remnants of fauna (e.g., orbitolinids) and oolitic and peloidal

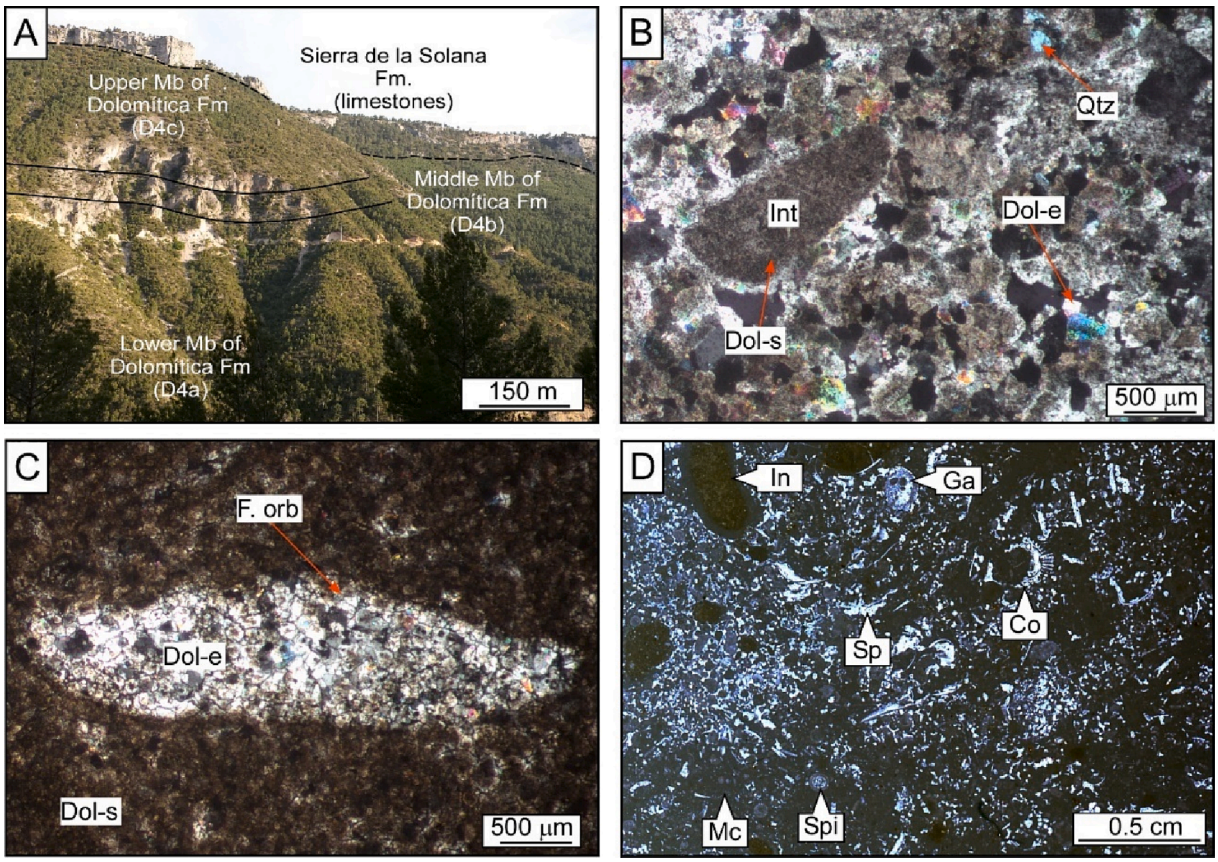

Fig. 10. Characteristics of the Upper Cretaceous stratabound dolomites (D4). A) Overview of the of discordant contact between the Sierra de la Solana limestone Fm. and the D4a, D4b and D4c stratabound dolostones of the Dolomítica Fm. B) Transmitted light with parallel polarizer (TL-PP) microphotograph of planar-s and planar-e dolomites from Lower Mb. of the Dolomítica Fm. (D4a) with intraclasts and detrital quartz. C) TL-PP microphotograph of planar-s and planar-e dolomites from Lower Mb. of the Dolomítica Fm. (D4a) with orbitolinid ghosts. D) TL-PP microphotograph of intramicritic packstone. Dol-s: anhedral to subhedral dolomite; Dol-e: euhedral dolomite; In: intraclast; F. orb: orbitolinid ghost; Ga: gastropod; Co: coral; Sp: sparite; Spi: echinoderm spicule; Mc: calcite microcrystalline matrix (micrite).

ghosts observed in thin section indicate that the Riópar dolostones replace original marine limestones (Figs. 6 to 10). The relatively high values of carbon and oxygen isotopes, as well as the relatively low ratios of strontium isotopic data, support a seawater dolomitization model for the large D1, D2 and D4 stratabound dolostone bodies (Figs. 11 to 13). However, this differs from the D3 stratabound dolostones connected by patchy geobodies hosted in the Upper Jurassic to Lower Cretaceous carbonate succession. A hydrothermal dolomitization model is favored for these D3 rocks (Figs. 11 to 13) based on their lower isotopic signature for C and O and the higher radiogenic ratios for Sr and is also supported by the isotopic modeling of water–rock interaction (Fig. 12).

The C and O isotopic values of the D1, D2 and D4 dolostones are similar to data of the Riópar Jurassic to Cretaceous host limestones (Figs. 11 and 12). Furthermore, $^{87}Sr/^{86}Sr$ ratios of these stratabound dolostones is also close to the Riópar regional limestones Sr isotopic composition (Figs. 11 and 13). Nevertheless, D4a dolostones show a slightly more radiogenic Sr isotopic values (Fig. 11), which may be due to the presence of terrigenous detritus components identified under a microscope (Fig. 10). This supports a seawater dolomitization (SWD) model, which typically involve low precipitation temperatures (Warren, 2000). Furthermore, this low temperature is consistent with the absence of Zn-(Fe-Pb) MVT mineralization and saddle dolomite formation. The three barren stratabound dolostone geobodies (D1, D2 and D4; Fig. 2) formed under seawater influence, were probably generated just after the diagenesis of host limestones, as stylolite formation (Fig. 6) occurred prior to dolomitization.

The C and O isotope distribution of D3 stratabound and patchy dolomitized limestones depicts a horizontal trend with a small shift in $\delta^{13}C$ (≈ 2‰) and $\delta^{18}O$ (≈ 3.5‰; Fig. 12). Compared to the host limestone and marine stratabound dolostones, these dolomites show relatively depleted $\delta^{13}C$ and $\delta^{18}O$ values (Figs. 11 and 12). This distribution can be modeled from an interaction of regional carbonates ($\delta^{13}C_{VPDB}$: +2.3‰; $\delta^{18}O_{VSMOW}$: +28.3‰) with a hydrothermal fluid ($\delta^{13}C_{VPDB}$: −8‰; $\delta^{18}O_{VSMOW}$: +17‰). Assuming an open system and using the equations of Zheng and Hoefs (1993), dolomite isotope data is consistent with the interaction between fluids with a CO_2 content of 0.1 M at a temperature range between 190 and 230 °C (Fig. 12). The carbon dominant species in the fluid was assumed to be H_2CO_3 and the fractionation equation of the isotopes between water and dolomite was taken from Land (1983) and between H_2CO_3 and dolomite from Chacko et al. (1991). $\delta^{13}C$ and $\delta^{18}O$ values of D3 dolostones indicate that low volumes of the hydrothermal fluid interacted with the limestones (between 3 and 10%; Fig. 12). Microthermometrical data from D3 stratabound and patchy dolostones (homogenization temperature: 150–250 °C; salinity: 5–25 wt% eq. NaCl; Navarro-Ciurana et al., 2016a) supports the presence of warm dolomitizing and mineralizing brines. Consequently, C and O isotope values can be used to differentiate between marine dolostones and HTDs, which may be fertile or barren (Fig. 12). $^{87}Sr/^{86}Sr$ isotopic ratios of HTDs range between values close to Jurassic to Cretaceous limestones and more radiogenic values (Figs. 11 and 12). Although the $^{87}Sr/^{86}Sr$ signature of HTDs are similar of host limestones, their combination with O isotopes allows again to distinguish the source of dolomitizing fluids (Figs. 12 and 13), although not their fertile or barren character.

Commonly, modern hydrothermal fluids have positive $(Eu/Eu^*)_{PAASN}$ and REE_{CN} profiles that are enriched in LREE (Fig. 15d; Bao

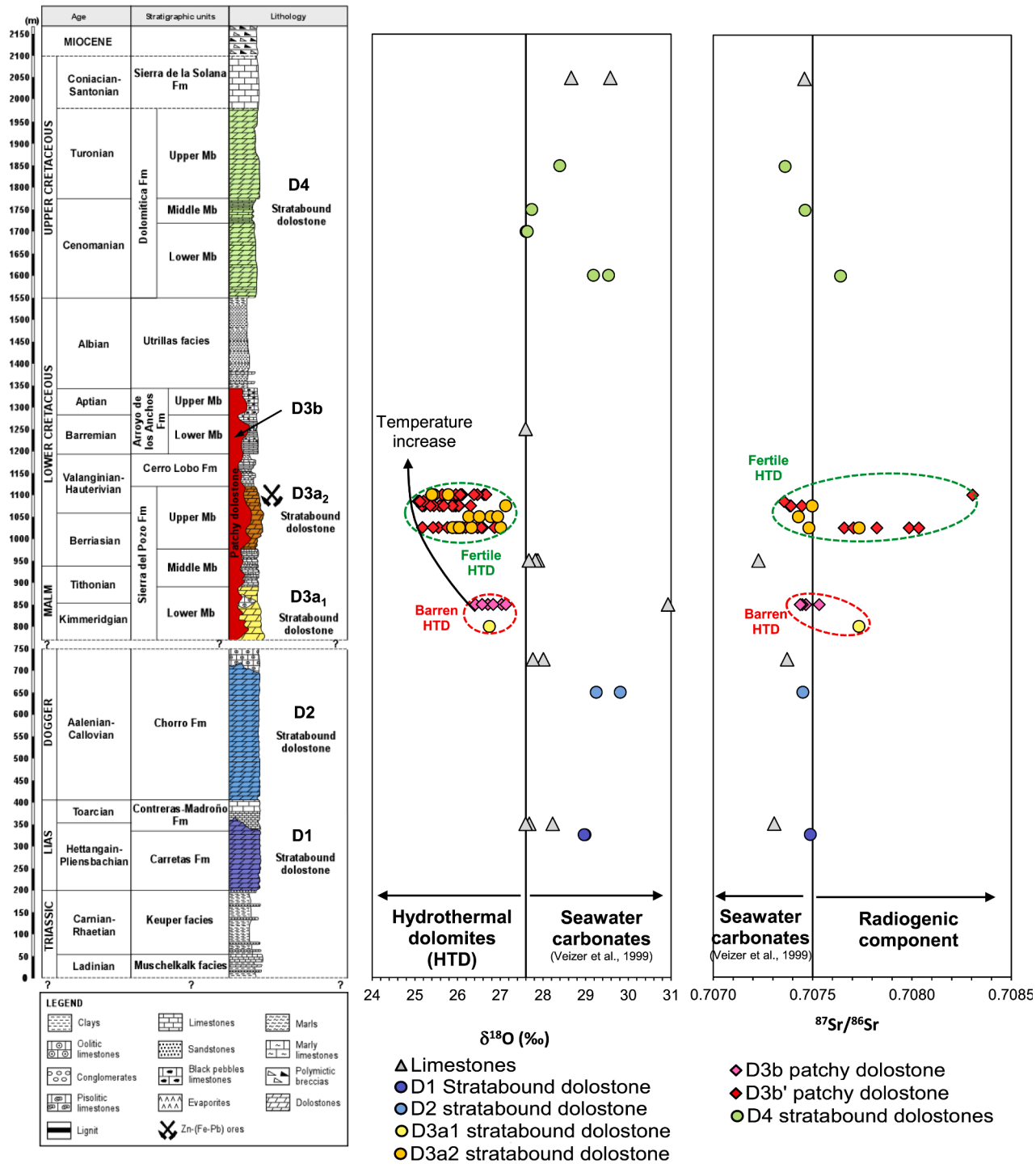

Fig. 11. Stratigraphic variation in oxygen and strontium isotopic compositions of carbonates from the Riópar area. Box of seawater carbonates indicates the range of Jurassic to Cretaceous marine carbonate according to Veizer et al. (1999). D1: Lower Jurassic stratabound dolostones (Carretas Fm.); D2: Middle Jurassic stratabound dolostones (Chorro Fm.); $D3a_1$: Upper Jurassic stratabound dolostones (Lower Mb. of Sierra del Pozo Fm.); $D3a_2$: Lower Cretaceous stratabound dolostone (Upper Mb. of Sierra del Pozo Fm.); D3b: Upper Jurassic patchy dolostones (Lower Mb. of Sierra del Pozo Fm.); D3b': Lower Cretaceous patchy dolostones (Upper Mb. of Sierra del Pozo Fm.); D4: Upper Cretaceous stratabound dolostones (Dolomítica Fm.).

et al., 2008; Craddock et al., 2010). These REE characteristics has been interpreted as a result of plagioclase dissolution during interaction of fluids with crustal rocks (e.g., Klinkhammer et al. 1994; Douville et al. 1999). Thus, the LREE enriched pattern of a chondrite-normalized REE plot (Fig. 14) and the positive $(Eu/Eu^*)_{PAASN}$ anomalies (Table 2 and Fig. 15) of the D3 stratabound and patchy dolostones suggest a hydrothermal origin for these dolomites. Moreover, the observed MREE enrichment pattern in PAAS-normalized REE pattern of the studied D3 dolostones (Fig. 15) suggests the involvement of acidic hydrothermal fluids during dolostone formation (Bau and Dulski, 1999). Eu^{2+} is more soluble than Eu^{3+} in Cl^- rich fluids under relatively high fO_2, acidic conditions and temperatures above 200–250 °C (Bau and Möller, 1992; Sverjensky, 1984; Bau, 1991; Migdisov et al. 2009; Craddock et al. 2010; Williams-Jones et al., 2012). This temperature range is consistent with the homogenization temperatures obtained in fluid inclusions (150–250 °C) of the Riópar D3 stratabound and patchy dolostones

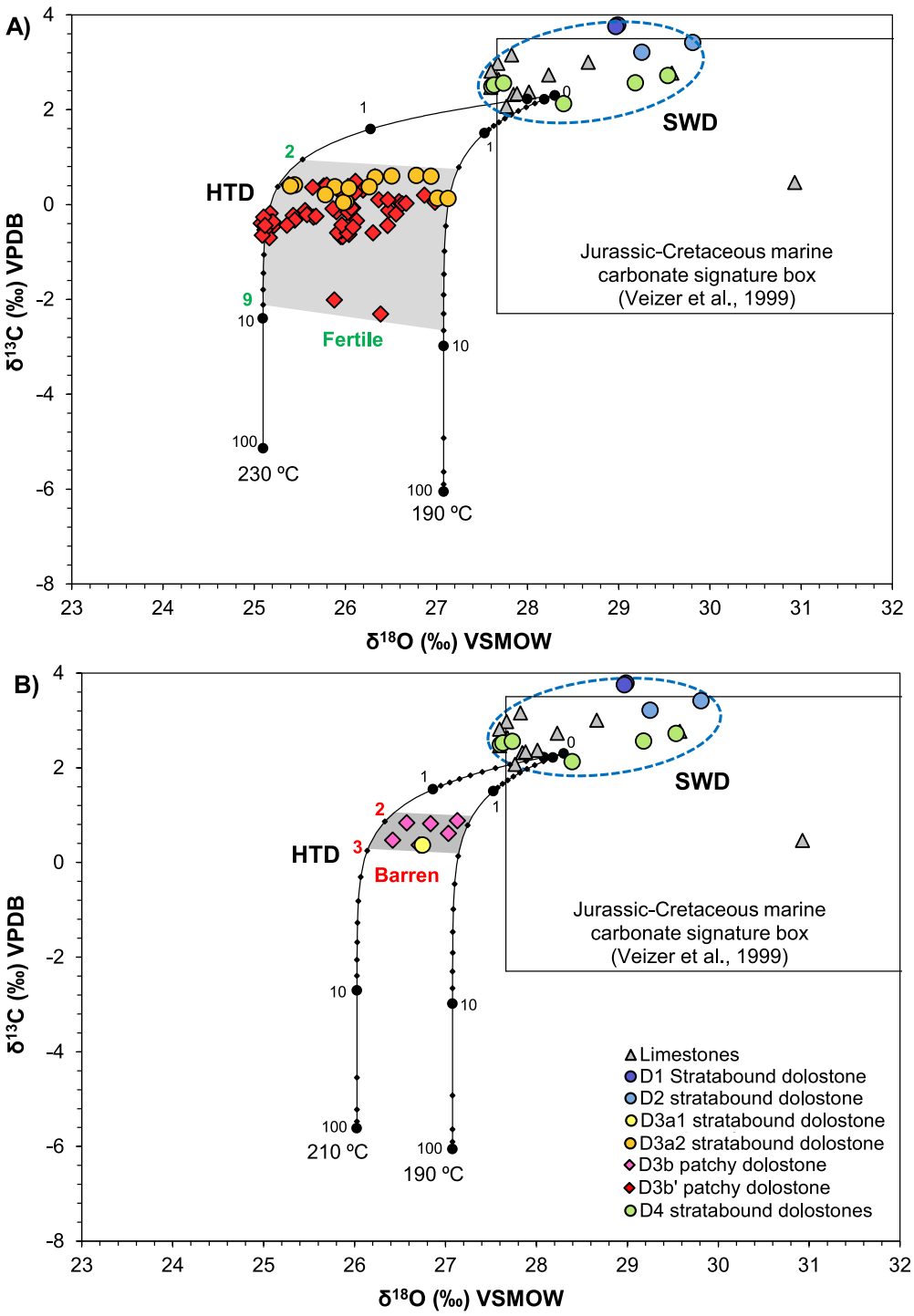

Fig. 12. $\delta^{13}C$ vs $\delta^{18}O$ cross-plot of host limestones, D1, D2 and D4 barren stratabound dolostones and D3 hydrothermal fertile (A) and barren (B) dolostones (HTD: hydrothermal dolomites; SWD: seawater dolomite). The upper corner box indicates the range of Jurassic to Cretaceous marine carbonate according to Veizer et al. (1999). C-O isotope model curves were calculated in terms of fluid-rock interaction for dolomite (continuous dark coarse lines) at temperatures of 230 °C, 210 °C and 190 °C (see Zheng and Hoefs, 1993). D1: Lower Jurassic stratabound dolostones (Carretas Fm.); D2: Middle Jurassic stratabound dolostones (Chorro Fm.); D3a1: Upper Jurassic stratabound dolostones (Lower Mb. of Sierra del Pozo Fm.); D3a2: Lower Cretaceous stratabound dolostone (Upper Mb. of Sierra del Pozo Fm.); D3b: Upper Jurassic patchy dolostones (Lower Mb. of Sierra del Pozo Fm.); D3b': Lower Cretaceous patchy dolostones (Upper Mb. of Sierra del Pozo Fm.); D4: Upper Cretaceous stratabound dolostones (Dolomítica Fm.).

(Navarro-Ciurana et al., 2016a).

On the other hand, all HTDs show $(Ce/Ce^*)_{PAASN}$ values comprised between 0.64 and 0.97, indicating a slightly negative Ce anomaly, and $(Pr/Pr^*)_{PAASN}$ values from 0.96 and 1.11, which are characteristic of no anomaly of Pr (Table 2 and Fig. 15). Ce is very sensitive to redox conditions, and soluble Ce^{3+} can be oxidized to Ce^{4+} that is less soluble but more diffusive in seawater (De Baar et al.,1991; Alibo and Nozaki, 1999), and consequently Ce^{4+} can be adsorbed on the sedimentary particle surface or precipitated as Ce-bearing minerals (Fe-hydroxides; e.g., Wang et al., 2014). This process reflects a cerium fractionation in seawater environment: the well-oxygenated seawater achieves a negative Ce anomaly (Alibo and Nozaki, 1999; Frimmel, 2009). Therefore, negative Ce anomalies in carbonate sediments and rocks (0.2–0.5) formed by diagenetic fluids are a robust indication that they were formed by cold seawater (Elderfield and Greaves, 1982; Piepgras and Jacobsen, 1992; Alibo and Nozaki, 1999; Osborne et al., 2014). On the other hand, hydrothermal fluids show near non-Ce (0.6 to 1.2) and non-Pr (0.8 to 1.2) anomalies (Alibo and Nozaki, 1999; Osborne et al., 2014). Consequently, if the dolomitizing fluid had originally been seawater, as is the most plausible explanation according to several models (e.g., Gómez-Rivas et al., 2014; Benjakul et al., 2020), it would have lost its REE signature during previous heating and interaction with other deeper rocks, acquiring the new ones of a hydrothermal fluid.

Although $(Ce/Ce^*)_{PAASN}$ and $(Pr/Pr^*)_{PAASN}$ values in carbonates (e.

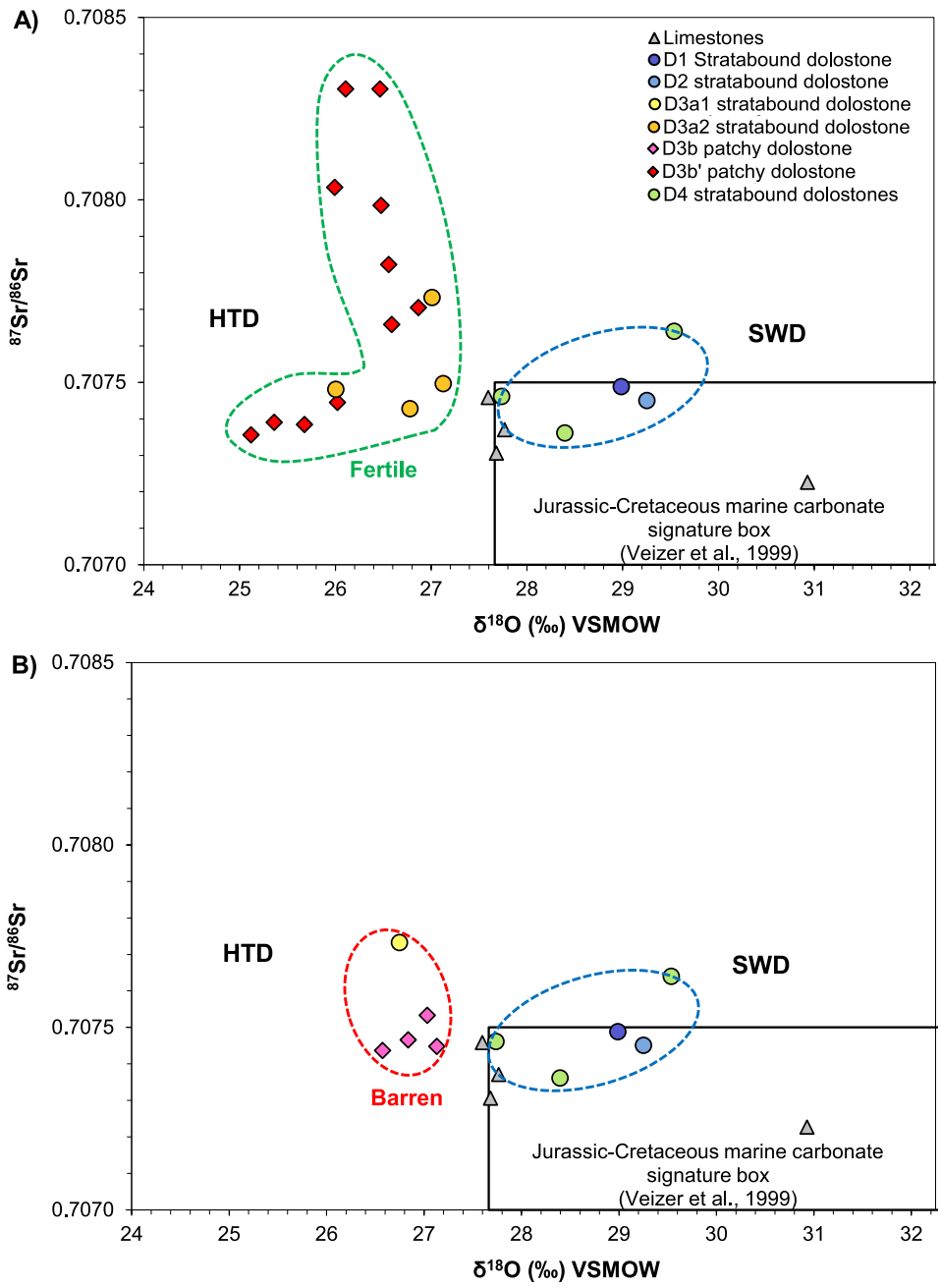

Fig. 13. $\delta^{18}O$ and $^{87}Sr/^{86}Sr$ plot of host limestone, D1, D2 and D4 barren stratabound dolostones and D3 fertile (A) and barren (B) dolostones (HTD: hydrothermal dolomites; SWD: seawater dolomite). The lower corner box indicates Middle Jurassic to Lower Cretaceous marine carbonate according to Veizer et al. (1999). D1: Lower Jurassic stratabound dolostones (Carretas Fm.); D2: Middle Jurassic stratabound dolostones (Chorro Fm.); D3a1: Upper Jurassic stratabound dolostones (Lower Mb. of Sierra del Pozo Fm.); D3a2: Lower Cretaceous stratabound dolostone (Upper Mb. of Sierra del Pozo Fm.); D3b: Upper Jurassic patchy dolostones (Lower Mb. of Sierra del Pozo Fm.); D3b': Lower Cretaceous patchy dolostones (Upper Mb. of Sierra del Pozo Fm.); D4: Upper Cretaceous stratabound dolostones (Dolomítica Fm.).

g., dolomite, calcite) have been used to discriminate their hydrothermal or low temperature seawater origin, the compositional fields of HTDs and low temperature dolomites have never before been defined in a $(Ce/Ce^*)_{PAASN}$ vs. $(Pr/Pr^*)_{PAASN}$ plot. This is what is presented in Fig. 16 with more than 1,500 values of $(Pr/Pr^*)_{PAASN}$ and $(Ce/Ce^*)_{PAASN}$ data being plotted from worldwide HTDs and low temperature seawater dolomites (Xuefeng et al., 2008; Azomani et al., 2013; Zhao and Jones, 2013; Wang et al., 2014; Hou et al., 2016; Li et al., 2016; Tortola et al., 2020; Chang et al., 2020; Xiang et al., 2020; Huang et al., 2022), as well as the compositional fields of present day hydrothermal fluids and seawater (Alibo and Nozaki, 1999; Bao et al., 2008; Craddock et al., 2010; Osborne et al., 2014). All data fit into a decreasing exponential function: $(Ce/Ce^*) = 40.9^{-3.9(Pr/Pr^*)}$, with a relatively good correlation of 0.82 (Fig. 16). For instance, dolostones of Cayman Brac (British West Indies; Zhao and Jones, 2013) show $(Pr/Pr^*)_{PAASN}$ and $(Ce/Ce^*)_{PAASN}$ values that plot in the field of present day seawater, indicating that they were formed by low-temperature marine fluids. On the other hand, $(Pr/Pr^*)_{PAASN}$ and $(Ce/Ce^*)_{PAASN}$ data of Panlongdong and Tarim basin dolostones (China: Xuefeng et al., 2008; Wang et al., 2014) plot between the defined fields of present day seawater and hydrothermal fluids (Fig. 16), demonstrating that they were either formed by a mixing of both fluid types or were originally seawater that acquired the characteristics of a hydrothermal fluid. The studied D3 Riópar dolostones have $(Pr/Pr^*)_{PAASN}$ and $(Ce/Ce^*)_{PAASN}$ values plotting with present day hydrothermal fluids, as occurs with a large variety of dolostones studied in other sites, such as Breno and Esino dolostones (Italy: Hou et al., 2016), Huron Domain, Newfoundland and Labrador dolostones (Canada: Azomani et al., 2013; Tortola et al., 2020), and Geshan, Jizhong and Yangtze Platform dolostones (China: Wang et al., 2014; Huang et al., 2022; Xiang et al., 2020; Chang et al., 2020).

Although, the Riópar D3 dolostones have $(Ce/Ce^*)_{PAASN}$ and $(Pr/Pr^*)_{PAASN}$ values typical of dolostones formed under hydrothermal conditions, in Fig. 16 they trend towards the seawater dolomite compositional field. This pattern can reflect several possibilities: i) a

Table 2
Minor and rare earth elements (REE) concentration of hydrothermal dolostones, including barren patchy and fertile stratabound and patchy types.

	Z01-(03)	Z01-(04)	Z01-(05)	Z01-(06)	SG02b-(07)	SG02b-(14)	SG04c-(01)	SG05-(02)	JO17-(07)	JO18-(01)	SG02a-(01)	SG05-(01)	SJ40-(01)
	Barren patchy dolomite (Lower Mb., Sierra del Pozo Fm.)				Fertile patchy dolomite (Upper Mb., Sierra del Pozo Fm.)						Fertile stratabound dolomite (Upper Mb., Sierra del Pozo Fm.)		
Pb (mg kg^{-1})	< 5	< 5	< 5	< 5	15	13	15	37	12	11	15	13	16
Y	1.9	1.5	1.7	1.3	6.4	3.1	5.8	3.7	1.6	1.1	12.6	3.1	6.1
Zn	80	150	80	80	>10000	1970	>10000	>10000	500	160	4580	2000	>10000
La	1.68	1.9	1.44	1.37	6.79	3.28	4.9	5.29	3.8	5.07	11.8	3.3	9.03
Ce	2.68	2.92	1.56	2.11	11	5.42	5.68	8.17	8.13	9.05	19.1	5.5	14
Pr	0.34	0.35	0.18	0.25	1.4	0.61	0.85	0.96	1.01	0.9	2.59	0.64	1.49
Nd	1.35	1.31	0.75	0.98	5.81	2.54	3.48	3.68	4.07	3.11	10.5	2.56	5.99
Sm	0.28	0.25	0.12	0.15	1.18	0.53	0.7	0.73	0.79	0.47	2.29	0.56	1.15
Eu	0.077	0.061	0.03	0.037	0.29	0.143	0.175	0.197	0.177	0.116	0.48	0.149	0.293
Gd	0.29	0.19	0.12	0.14	1.13	0.54	0.78	0.73	0.45	0.29	2.07	0.58	1.11
Tb	0.04	0.03	0.02	0.03	0.16	0.08	0.1	0.09	0.06	0.04	0.32	0.08	0.16
Dy	0.23	0.17	0.13	0.15	0.84	0.44	0.55	0.48	0.25	0.19	1.9	0.43	0.82
Ho	0.04	0.03	0.03	0.03	0.16	0.08	0.13	0.09	0.04	0.03	0.36	0.08	0.15
Er	0.12	0.09	0.09	0.08	0.45	0.22	0.39	0.24	0.1	0.08	1.06	0.23	0.41
Tm	0.016	0.012	0.013	0.011	0.062	0.028	0.054	0.03	0.013	0.012	0.161	0.031	0.056
Yb	0.1	0.06	0.07	0.06	0.36	0.16	0.31	0.17	0.07	0.07	1.01	0.19	0.32
Lu	0.016	0.008	0.011	0.008	0.053	0.024	0.048	0.028	0.011	0.012	0.146	0.03	0.046
$\sum REE^{1}$	7.26	7.38	4.56	5.41	29.69	14.10	18.15	20.89	18.97	19.44	53.79	14.36	35.03
$\sum LREE^{2}$	6.41	6.79	4.08	4.90	26.47	12.52	15.79	19.03	17.98	18.72	46.76	12.71	31.95
$\sum HREE^{3}$	0.85	0.59	0.48	0.51	3.22	1.57	2.36	1.86	0.99	0.72	7.03	1.65	3.07
La_{CN}/Sm^{4}_{CN}	3.78	4.78	7.55	5.75	3.62	3.90	4.41	4.56	3.03	6.79	3.24	3.71	4.94
La_{CN}/Yb^{5}_{CN}	11.35	21.40	13.90	15.43	12.75	13.85	10.68	21.03	36.68	48.94	7.89	11.74	19.07
Sm_{CN}/Yb^{6}_{CN}	3.01	4.47	1.84	2.68	3.52	3.56	2.42	4.61	12.12	7.21	2.43	3.16	3.86
$(Ce/Ce^{*})^{7}_{CN}$	0.79	0.79	0.62	0.79	0.80	0.85	0.61	0.80	0.96	0.93	0.78	0.84	0.82
$(Eu/Eu^{*})^{8}_{CN}$	0.82	0.82	0.76	0.77	0.76	0.81	0.72	0.82	0.83	0.89	0.66	0.79	0.78
$(Ce/Ce^{*})^{9}_{PAASN}$	0.82	0.82	0.67	0.83	0.82	0.88	0.64	0.83	0.96	0.97	0.80	0.87	0.87
$(Pr/Pr^{*})^{10}_{PAASN}$	1.05	1.05	0.98	1.02	1.02	0.97	1.11	1.03	1.03	0.99	1.07	1.00	0.96
$(Eu/Eu^{*})^{11}_{PAASN}$	1.27	1.32	1.17	1.20	1.18	1.25	1.10	1.27	1.37	1.46	1.04	1.22	1.22

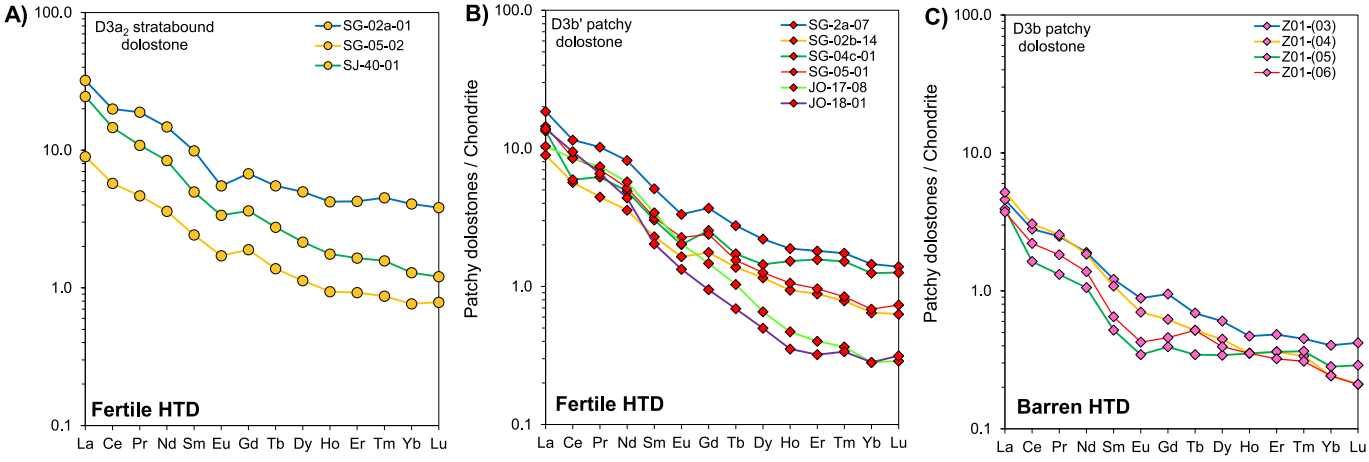

Fig. 14. Chondrite-normalized REE distributions of D3 hydrothermal dolostones (HTD: Upper Jurassic-Lower Cretaceous). A) Mineralized $D3a_2$ stratabound dolostones (fertile) hosted in Upper Mb. of the Sierra del Pozo Fm. B) Mineralized D3b' patchy dolostones (fertile) hosted in Upper Mb. of the Sierra del Pozo Fm. C) Barren D3b patchy dolostones hosted in Lower Mb. of the Sierra del Pozo Fm. See Fig. 3 for sample location. Normalization values after McDonough and Sun (1995).

mixing of the hydrothermal fluid with some contribution of cold seawater fluids (maybe preserved in the porosity of the limestone) during the formation of hydrothermal dolostones, which is consistent with fluid inclusion microthermometric data suggesting fluid mixing (Navarro-Ciurana et al., 2016a); ii) a partial preservation of negative Ce anomaly from the precursor marine host limestones, due to the low volume of hydrothermal fluid interaction with marine carbonates, which is consistent with the obtained $\delta^{13}C$ and $\delta^{18}O$ values in the studied HTDs; and/or iii) a preservation of the original seawater REE signature (negative Ce anomaly) by the hydrothermal fluid (positive Eu anomaly; Fig. 15). In any case, $(Ce/Ce^{*})_{PAASN}$ and $(Pr/Pr^{*})_{PAASN}$ values, as well as $(Eu/Eu^{*})_{PAASN}$, $\delta^{13}C$ and $\delta^{18}O$ data, allow to differentiate unmineralized SWDs from HTDs, which can be unmineralized (barren) or mineralized (fertile) (Figs. 11, 12 and 16). From all the data gathered, it is observed that dolomite values of $(Ce/Ce^{*})_{PAASN}$ larger than 0.55 imply that they are HTDs, whereas values lower than 0.50 indicate that they are SWDs.

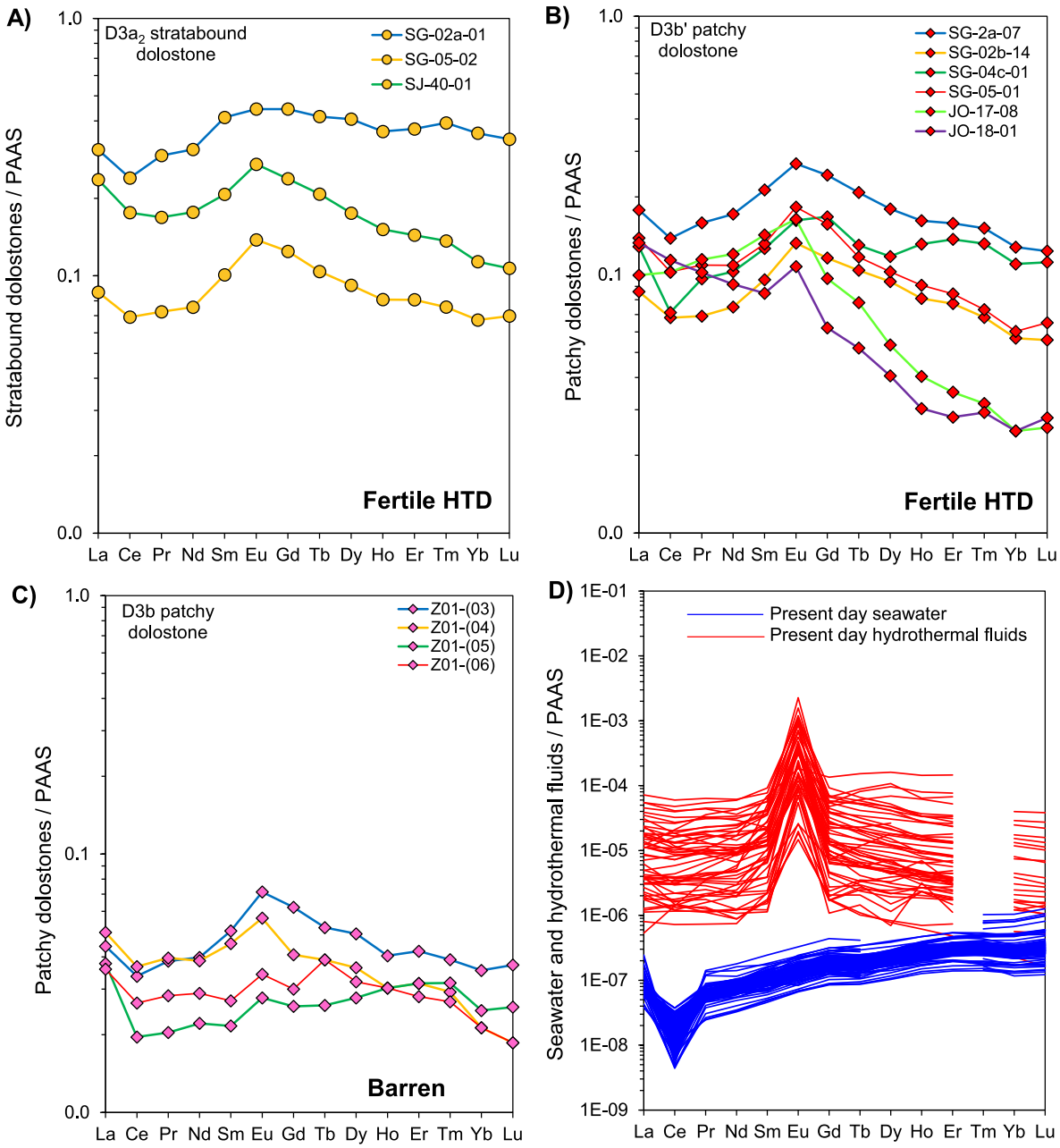

Fig. 15. Post Archean Australian Shale (PAAS)-normalized REE distributions of D3 hydrothermal dolostones (HTD: Upper Jurassic-Lower Cretaceous). A) Mineralized D3a2 stratabound dolostones (fertile) hosted in the Upper Mb. of the Sierra del Pozo Fm. B) Mineralized D3b' patchy dolostones (fertile) hosted in the Upper Mb. of the Sierra del Pozo Fm. C) Barren D3b patchy dolostones hosted in the Lower Mb. of the Sierra del Pozo Fm. D) Present day seawater and hydrothermal fluids (data from: Alibo and Nozaki, 1999; Bao et al., 2008; Craddock et al., 2010; Osborne et al., 2014). See Fig. 3 for sample location. Normalization values after Taylor and McLennan (1985).

2.2. *Discriminating barren from mineralized HTDs*

Whereas strontium isotopes may be similar in limestones and dolostones of different origins, it has been demonstrated that carbon and oxygen, as well as $(Ce/Ce^*)_{PAASN}$, $(Pr/Pr^*)_{PAASN}$ and $(Eu/Eu^*)_{PAASN}$ values, discriminate between SWDs, formed from cold seawater that do not host MVT mineralization, from HTDs, which can host Zn-Pb MVT mineralization. Nevertheless, one of the major challenges when investigating and exploring for economic MVT deposits in carbonate-rich systems is to quickly discriminate between barren and fertile dolomites both formed under hydrothermal conditions. In the Riópar case, where D3 HTDs extensively replace the Upper Jurassic to Lower Cretaceous carbonate sequence (Fig. 11), Zn-(Fe-Pb) mineralization is only hosted in hydrothermal patchy (D3b) and stratabound dolostones of the Lower Cretaceous carbonates ($D3a_2$, Fig. 11). Although barren HTDs show more restricted C, O and Sr isotope values than mineralized HTDs (Figs. 12 to 14), possibly due to lower fluid/rock interaction (2 to 3% of fluid, Fig. 13b), there is an isotopic overlap between both HTD types. In the Riópar area, barren HTDs show lower total REE concentrations (4.56 to 7.38 mg kg^{-1}) and higher $\delta^{13}C$ values (+0.4 to + 0.9‰) than fertile dolostones ($\sum$HREE = 14.36 – 53.79 mg kg^{-1}, $\delta^{13}C$ = -2.3 to + 0.6‰). Plots between REE total content and $\delta^{13}C$ values of HTDs seem to be a promising tool for discriminating mineralized from barren HTDs (Fig. 17). The abovementioned overlap in the C isotopic signature of unmineralized and mineralized HTDs is not reflected in Fig. 17 as only a subset of representative samples was analyzed (for both $\delta^{13}C$ and REE)

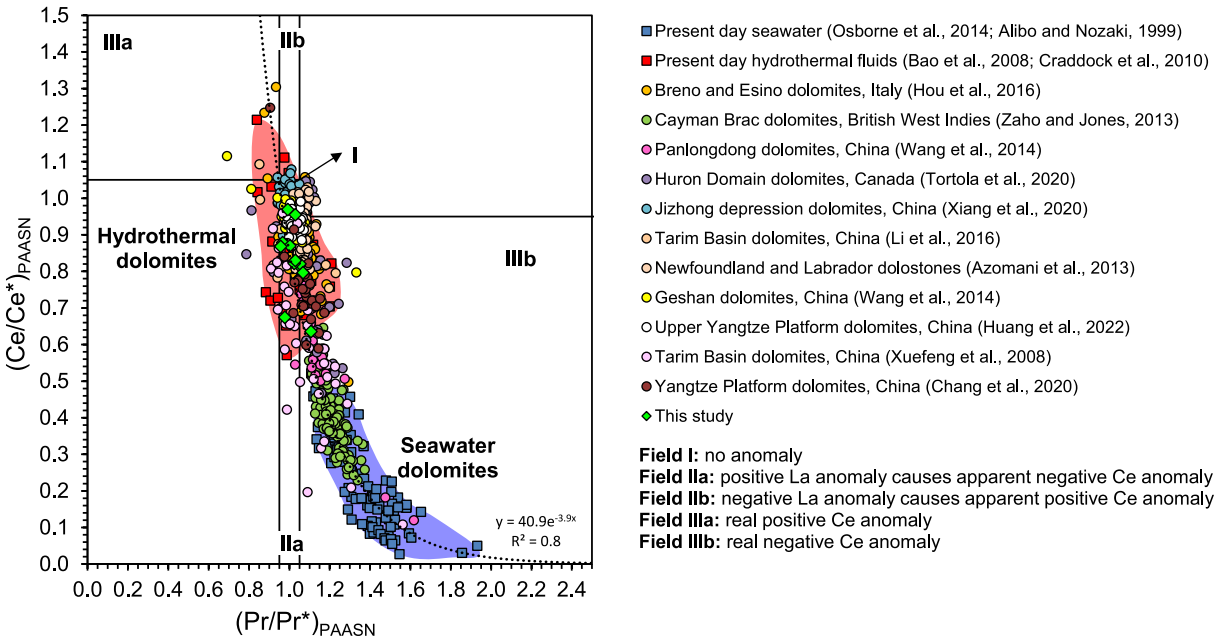

Fig. 16. Cross plot of Post Archean Australian Shale (PAAS)-normalized $(Pr/Pr^*)_{PAASN}$ versus $(Ce/Ce^*)_{PAASN}$ values (modified after Bau and Dulski, 1996) of the Riópar D3 stratabound and patchy dolostones (this study). Present day seawater and hydrothermal data (Alibo and Nozaki, 1999; Bao et al., 2008; Craddock et al., 2010; Osborne et al., 2014), as well as worldwide dolostones (Xuefeng et al., 2008; Azomani et al., 2013; Zhao and Jones, 2013; Wang et al., 2014; Hou et al., 2016; Li et al., 2016; Tortola et al., 2020; Chang et al., 2020; Xiang et al., 2020; Huang et al., 2022), are represented. Blue and red color areas correspond to present day seawater and hydrothermal fluids, respectively. Global dolostones are distributed according the $(Ce/Ce^*) = 40.9–3.9(Pr/Pr^*)$ function (dashed line).

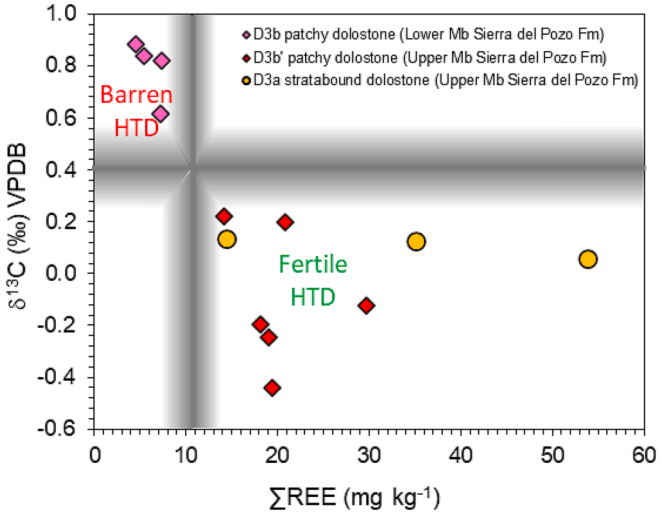

Fig. 17. Plot of ∑REE (mg kg^{-1}) vs. $\delta^{13}C$ (‰) for the Riópar D3 hydrothermal dolostones. The barren hydrothermal dolomites show lower concentrations of REE and higher $\delta^{13}C$ values than the mineralization fertile hydrothermal dolomites. The blurred gray lines tentatively indicate the boundary between fertile and barren dolostones.

and subsequently plotted. This is the main limitation of the tentatively proposed fertile/barren fields of the $\delta^{13}C$ vs. total REE plot which would be better constrained with a larger dataset.

The different REE concentration between mineralized and unmineralized hydrothermal host carbonates is similarly recorded in other MVT deposits. For example, Nejadhadad et al. (2016) identified that unmineralized and mineralized carbonates of the MVT Ravanj deposit (Iran) are characterized by positive Eu anomalies, suggesting that both are formed under hydrothermal conditions, but the obtained ∑HREE values of the unmineralized carbonates are lower (2.49 to 2.95 mg kg-1) than the ones mineralized (13.03 to 29.68 mg kg^{-1}), which are in the range of the results presented here. The discrimination between mineralized and unmineralized HTDs by means of REE concentration is also reflected in the Zn and Pb contents of dolostones: barren HTDs, which are located proximal to the Socovos fault (Fig. 3), have Pb concentration below the detection limit and very low Zn content (80–150 mg kg^{-1}), whereas weakly mineralized HTDs, as well as the HTDs hosting the ore body lenses, have higher Pb (11–16 mg kg^{-1}) and Zn (up to 10,000 mg kg^{-1}; Table 2) contents. The fertile dolostones and Zn-(Fe-Pb) deposits appear nearer the San Jorge fault (Fig. 3); so that the hydrothermal dolomitizing fluid flowed from the San Jorge fault towards the Socovos fault, interacting more intensely with the rocks nearer the former. In the vicinity of the San Jorge fault the hydrothermal fluid, enriched in metals (e.g., Zn, Fe, Pb), interacted with the host limestones at higher temperatures (190 to 230 °C) and higher fluid/rock ratios (F/R: 2–10%) than further away (190 to 210 °C; F/R: 2–3%).

2.3. Applicability of the new geochemical tool for MVT exploration

Field observations and petrographic characterization do not stand alone as a discrimination tool for dolostone's origin, nor their fertility as shown in the Riópar area. Microthermometry of fluid inclusions in all dolostone geobodies would differentiate their origin (cold seawater from warm brine) by determining the minimum formation temperature and the salinity of the dolomitizing fluids. However, such a work first requires good samples (with large fluid inclusions) and then long periods of time to carry out sample preparation (double-polished thin section) and the microthermometric study. Instead, stable (C, O) isotope geochemistry turned out to be a useful technique to discriminate the dolomitic unit's origin (cold seawater/hydrothermal; Fig. 12). Similarly, for the geochemical study (REE) only a small volume of sample is needed with a short preparation time. Its outcome coupled with stable isotope results (C, O) is effective discriminating between fertile and barren HTDs in a relatively shorter periods of time, resulting in a time-efficient exploration tool.

In order to apply this geochemical tool, it is necessary to sample the precursor non-dolomitized limestones and the different types of existing

dolomites to determine the C and O isotope composition. These values would then be compared with the theoretical $\delta^{13}C$ and $\delta^{18}O$ compositions for seawater at the corresponding formation age (see Veizer, 1999 for Phanerozoic seawater C and O isotope compositions): if the dolomite $\delta^{13}C$ and $\delta^{18}O$ values are in the range of precursor non-dolomitized limestones and the assumed theoretical C and O isotope values of ancient seawater, the geobody dolomite will be classified as unmineralized (barren) seawater dolomite (SWD). This approach will be complemented with dolomite $\sum$REE concentrations, and specifically with Eu/Eu*, Ce/Ce* and Pr/Pr* values normalized to PAAS. HTDs will be characterized by positive $(Eu/Eu^*)_{PAASN}$ anomalies, whereas barren SWDs by negative $(Ce/Ce^*)_{PAASN}$ anomalies. Afterwards, coupling the HTDs $\delta^{13}C$ data with their $\sum$REE data will allow to effectively discriminate between fertile and barren HTDs (Fig. 17). Fields of fertile/barren HTDs have been tentatively constrained considering that fertile HTDs contain higher $\sum$REE concentration (>10–13 mg kg^{-1}) than barren HTDs (<8–10 mg kg^{-1}). Finally, as double-check procedure, $\sum$REE concentration of HTDs can be compared with whole-rock geochemical data as fertile HTDs systematically show much higher concentration of Zn and Pb than barren HTDs.

3. Conclusions

A new geochemical tool for MVT has been developed in the Riópar area (SE Spain), a district that contains some of the oldest Zn-Pb MVT mines of Europe. A large section of Mesozoic carbonates with different types of dolostones outcrops in the zone, where mineralization is hosted in hydrothermal dolomites that are petrographically indistinguishable from non-mineralized dolomites. However, they show significant geochemical differences as follows:

Low temperature dolostones which are not associated with MVT mineralization (barren) present $\delta^{13}C$ values comprised between +2.1 and +3.8‰ VPDB and $\delta^{18}O$ from +27.6 to +29.8‰ VSMOW. The isotopic composition is similar to marine host limestones and therefore formed by cold seawater. In comparison, hydrothermal dolostones show depleted $\delta^{13}C$ and $\delta^{18}O$ values with high $^{87}Sr/^{86}Sr$ compositions, that can be explained by the interaction of hydrothermal fluids (190–230 °C) with limestones.

Although hydrothermal dolostones preferentially replace limestones of Upper Jurassic to Lower Cretaceous age, not all this dolostone bodies host Zn-Pb mineralization. Barren hydrothermal dolostones are characterized by low $\sum$REE (5.41 to 7.38 mg kg^{-1}), Pb (<5 mg kg^{-1}) and Zn (80 to 150 mg kg^{-1}) content, and heavy $\delta^{13}C$ (+0.4 to +0.9 ‰ VPDB) and $\delta^{18}O$ values (+26.4 to +27.1 ‰ VSMOW).

Mineralized hydrothermal dolostones (fertile) show lighter $\delta^{13}C$ (−2.3 to +0.6 ‰ VPDB) and $\delta^{18}O$ values (+25.1 to +27.1 ‰ VSMOW), as well as higher concentration of $\sum$REE (14.10 to 54.79 mg kg^{-1}), Pb (11 to 37 mg kg^{-1}) and Zn (160 to up 10.000 mg kg^{-1}).

The newly proposed geochemical tool for Zn-Pb MVT mineral exploration couples $\delta^{13}C$, $\delta^{18}O$, (Ce/Ce*)PAASN and (Pr/Pr*)PAASN ratios, as well as dolomite $\sum$REE, to discriminate between mineralized (fertile) hydrothermal dolostones, unmineralized (barren) hydrothermal dolostones and barren cold seawater dolostones.

Declaration of Competing Interest

The authors declare that they have no known competing financial interests or personal relationships that could have appeared to influence the work reported in this paper.

Data availability

Data will be made available on request.

Acknowledgements

The authors would like to acknowledge Dr. Albert Griera, Dr. David Gómez-Gras (Universitat Autònoma de Barcelona) and Federico Ballesta (Ciencia y Aventura Company) for their help and assessment during fieldwork. The authors would like to acknowledge the technicians of the Laboratori de Preparació de Làmines Primes of Universitat Autònoma de Barcelona for their support in the preparation of thin sections, the Serveis Científics Tècnics of the Universitat de Barcelona and the Geochronology and the Isotope Geochemistry Centre of the Universidad Complutense de Madrid for their support during isotopic analysis. The authors are grateful to the AGAUR-SGR2017-1485 research group. We would like to thank Saulo de Oliveira and anonymous referee for their critical and valuable reviews, as well as to the Associated Editor Huayong Che for handling this manuscript.

Funding

Funding for this research was provided by the Spanish projects CGL2011-26488 and PID2019-109018RB-I00 to M. Corbella granted by the Spanish Ministerio de Economía y Competitividad and Ministerio de Ciencia e Innovación, respectivelly. Additional support was provided by the Universitat Autònoma de Barcelona and Universitat de Barcelona.

References

Alibo, D.S., Nozaki, Y., 1999. Rare earth elements in seawater: particle association, shale-normalization, and ce oxidation. Geochim. Cosmochim. Acta 63, 363–372. https://doi.org/10.1016/S0016-7037(98)00279-8.

Arias, C., Masse, J.P., Vilas, L., 1996. Relaciones tectónica-sedimentación en el Aptiense de la Sierra Larga, Jumilla (Murcia). Geogaceta 20 (1), 43–47.

Azéma, J., 1977. Étude géologique des zones externes des Cordilleres Bétiques aux confins des provinces d' Alicante et de Murcie (Espagne) VI, 393. Unpublished Ph.D. thesis.

Azomani, E., Azmy, K., Blamey, N., Brand, U., Al-Aasm, I., 2013. Origin of Lower Ordovician dolomites in eastern Laurentia: Controls on porosity and implications from geochemistry. Mar. Pet. Geol. 40, 99–114. https://doi.org/10.1016/j.marpetgeo.2012.10.007.

Banks, C.J., Warburton, J., 1991. Mid-crustal detachment in the Betic system of southeast Spain. Tectonophysics 191, 275–289. https://doi.org/10.1016/0040-1951(91)90062-W.

Banner, J.L., Hanson, G.N., Meyers, W.J., 1988. Rare earth element and Nd isotopic variations in regionally extensive dolomites from the Burlington-Keokuk Formation Mississippian: implications for REE mobility during carbonate diagenesis. J. Sediment Petrol 58, 415–432. https://doi.org/10.1306/212F8DAA-2B24-11D7-8648000102C1865D.

Bao, S.-X., Zhou, H.-Y., Peng, X.-T., Ji, F.-W., Yao, H.-Q., 2008. Geochemistry of REE and yttrium in hydrothermal fluids from the Endeavour segment, Juan de Fuca Ridge. Geochem. J. 42, 359–370. https://doi.org/10.2343/geochemj.42.359.

Barbero, L., López-Garrido, A.C., 2006. Mesozoic thermal history of the Prebetic continental margin (southern Spain): Constraints from apatite fission-track analysis. Tectonophysics 422, 115–128. https://doi.org/10.1016/j.tecto.2006.05.011.

Barker, S.L.L., Dipple, G.M., Hickey, K.A., Lepore, W.A., Vaughan, J.R., 2013. Applying stable isotopes to mineral exploration: teaching an old dog new tricks. Econ. Geol. 108, 1–9. https://doi.org/10.2113/econgeo.108.1.1.

Bau, M., 1991. Rare-earth element mobility during hydrothermal and metamorphic fluid-rock interaction and the significance of the oxidation state of europium. Chem. Geol. 93, 219–230. https://doi.org/10.1016/0009-2541(91)90115-8.

Bau, M., Dulski, P., 1996. Distribution of yttrium and rareearth elements in the Penge and Kuruman iron-formations, Transvaal Supergroup, South Africa. Precambrian Res. 79, 37–55. https://doi.org/10.1016/0301-9268(95)00087-9.

Bau, M., Möller, P., 1992. Rare earth element fractionation in metamorphogenic hydrothermal calcite, magnesite and siderite. Mineral. Petrol. 45, 231–246. https://doi.org/10.1007/BF01163114.

Behnsen, H., Spandler, C., Corral, I., Chang, Z., Dirks, P.H.G.M., 2021. Copper-gold fertility of arc volcanic rocks: a case study from the Early Permian Lizzie Creek Volcanic Group, NE Queensland, Australia. Econ. Geol. 116, 1141–1159. https://doi.org/10.5382/econgeo.4806.

Benjakul, R., Hollis, C., Robertson, H.A., Sonnenthal, E.L., Whitaker, F.F., 2020. Understanding controls on hydrothermal dolomitisation: insights from 3D Reactive Transport Modelling of geothermal convection. Solid Earth 11, 2439–2461. https://doi.org/10.5194/se-11-2439-2020.

Bierlein, F.P., Arne, D.C., Cartwright, I., 2004. Stable isotope (C, O, S) systematics in alteration haloes associated with orogenic gold mineralization in the Victorian gold province, SE Australia. Geochem. Explor. Environ Anal. 4, 191–211. https://doi.org/10.1144/1467-7873/04-201.

Boni, M., Parente, G., Bechstädt, T.h., De Vivo, B., Iannace, A., 2000. Hydrothermal dolomites in SW Sardinia (Italy): evidence for a widespread late-Variscan fluid flow

event. Sed. Geology 131, 181–200. https://doi.org/10.1016/S0037-0738(99)00131-1.
Chacko, T., Mayeda, T.K., Clayton, R.N., Goldsmith, J.R., 1991. Oxygen and carbon isotope fractionations between CO_2 and calcite. Geochim. Cosmochim. Acta 55, 2867–2882. https://doi.org/10.1016/0016-7037(91)90452-B.
Chang, Z., Hedenquist, J.W., White, N.C., Cooke, D.R., Roach, M., Deyell, C.L., Garcia, J. J., Gemmell, J.B., Mcknight, S., Cuison, A.L., 2011. Exploration tools fro linked porphyry and epithermal deposits: Example from the Manakayan intrusion-centered Cu-Au district, Luzon, Philippines. Econ. Geol. 106, 1365–1398. https://doi.org/10.2113/econgeo.106.8.1365.
Chang, B., Li, C., Liu, D., Foster, I., Tripati, A., Lloyd, M.K., Maradiaga, I., Luo, G., An, Z., She, Z., Xie, S., Tong, J., Huang, J., Algeo, T.J., Lyons, T.W., Immenhause, A., 2020. Massive formation of early diagenetic dolomite in the Ediacaran ocean: Constraints on the "dolomite problem" Earth Atmos. Planet. Sci. 117, 14005–14014. https://doi.org/10.1073/pnas.191667311.
Cook, N.J., Ciobanu, C.L., Pring, A., Skinner, W., Shimizu, M., Danyushevsky, L., Saini-Eidukat, B., Melcher, F., 2009. Trace and minor elements in sphalerite: a LA-ICPMS study. Geochim. Cosmochim. Acta 73, 4761–4791. https://doi.org/10.1016/j.gca.2009.05.045.
Cook, N.J., Ciobanu, C.L., Williams, T., 2011. The mineralogy and mineral chemistry of indium in sulphide deposits and implications for mineral processing. Hydrometall. 108, 226–228. https://doi.org/10.1016/j.hydromet.2011.04.003.
Coplen, T.B., Kendall, C., Hopple, J., 1983. Comparison of stable isotope reference samples. Nature 302, 236–238. https://doi.org/10.1038/302236a0.
Corral, I., Cardellach, E., Corbella, M., Canals, À., Griera, A., Gómez-Gras, D., Johnson, C. A., 2017. Origin and evolution of mineralizing fluids and exploration of the Cerro Quema Au-Cu deposit (Azuero Peninsula, Panama) from a fluid inclusion and stable isotope perspective. Ore Geol. Rev. 80, 947–960. https://doi.org/10.1016/j.oregeorev.2016.09.008.
Craddock, P.R., Bach, W., Seewald, J.S., Rouxel, O.J., Reeves, E., Tivey, M.K., 2010. Rare earth element abundances in hydrothermal fluids from the Manus Basin, Papua New Guinea: Indicators of sub-seafloor hydrothermal processes in back-arc basins. Geochim. Cosmochim. Acta 74, 5494–5513. https://doi.org/10.1016/j.gca.2010.07.003.
Davies, G.R., Smith, L.B., 2006. Structurally controlled hydrothermal dolomite reservoir facies: An overview. Am. Assoc. Pet. Geol. Bull. 90, 1641–1690. https://doi.org/10.1306/05220605164.
De Baar, H.J.W., Schijf, R.H., Byrne, R.H., 1991. Solution chemistry of the rare earth elements in seawater. Eur. J. Solid State Inorg. Chem. 28, 357–373.
Dewit, J., Foubert, A., El Desouky, H.A., Muchez, P., Hunt, D., Vanhaecke, F., Swennen, R., 2014. Characteristics, genesis and parameters controlling the development of a large stratabound HTD body at Matienzo (Ramales Platform, Basque-Cantabrian Basin, northern Spain). Mar. Pet. Geol. 55, 6–25. https://doi.org/10.1016/j.marpetgeo.2013.12.021.
Dickson, J.A.D., 1966. Carbonate identification and genesis as revealed by staining. J. Sediment. Res. 36, 491–505. https://doi.org/10.1306/74d714f6-2b21-11d7-8648000102c1865d.
Douville, E., Bienvenu, P., Charlou, J.L., Donval, J.P., Fouquet, Y., Appriou, P., Gamo, T., 1999. Yttrium and rare earth elements in fluids from various deep-sea hydrothermal systems. Geochem. Cosmochim. Acta 63, 627–643. https://doi.org/10.1016/S0016-7037(99)00024-1.
Duggan, J.P., Mountjoy, E.W., Stasiuk, L.D., 2001. Fault-controlled dolomitization at Swan Hills Simonette oil field (Devonian), deep basin west-central Alberta, Canada. Sedimentology 48, 301–323. https://doi.org/10.1046/j.1365-3091.2001.00364.x.
Elderfield, H., Greaves, M.J., 1982. The rare earth elements in seawater. Nature 296, 214–219. https://doi.org/10.1038/296214a0.
Erdmann, L., Graedel, T.E., 2011. Criticality of non-fuel minerals: a review of major approaches and analyses. Environ. Sci. Technol. 45, 7620–7630. https://doi.org/10.1021/es200563g.
EU Commission, 2020. Critical raw materials resilience: charting a path towards greater security and sustainability (Accessed on 1st September 2022, at https://ec.europa.eu/docsroom/documents/42849).
Fernández-Gianotti, J., Perucha, M.A., Benito, M.I., Rodríguez-Estrella, T., Nozal, F., Gómez-Fernández, J.J., Meléndez, J.J., Aragón, R., Hornero, J., 2001. Mapa Geológico de España 1:50.000, hoja n° 866 (Yeste). I.G.M.E Mem. 48, pp.
Frenzel, M., Hirsch, T., Gutzmer, J., 2016. Gallium, germanium, indium, and other trace and minor elements in sphalerite as a function of deposit type — A meta-analysis. Ore Geol. Rev. 76, 52–78. https://doi.org/10.1016/j.oregeorev.2015.12.017.
Friedman, G.M., 1965. Terminology of crystallization textures and fabrics in sedimentary rocks. J. Sediment. Petrol. 35, 643–655. https://doi.org/10.1306/74D7131B-2B21-11D7-8648000102C1865D.
García-Hernández, M., López-Garrido, A.C., Rivas, P., Sanz de Galdeano, C., Vera, J.A., 1980. Mesozoic paleogeographic evolution of the external zones of the Betic Cordillera. Geol. Mijnb. 50 (2), 155–168.
Gasparrini, M., Bechstädt, T., Boni, M., 2006. Massive hydrothermal dolomites in the southwestern Cantabrian Zone (Spain) and their relation to the Late Variscan evolution. Mar. Pet. Geol. 23, 543–568. https://doi.org/10.1016/j.marpetgeo.2006.05.003.
Gisbert, G., Tornos, F., Losantos, E., Pons, J.M., Videira, J.C., 2021. Vectors to ore in replacive volcanogenic massive sulfide (VMS) deposits of the northern Iberian Pyrite Belt: mineral zoning, whole rock geochemistry, and application of portable X-ray fluorescence. Solith Earth 12, 1931–1966. https://doi.org/10.5194/se-12-1931-2021.
Gomez-Rivas, E., Corbella, M., Martín-Martín, J.D., Stafford, S.L., Teixell, A., Bons, P.D., Griera, A., Cardellach, E., 2014. Reactivity of dolomitizing fluids and Mg source evaluation of fault-controlled dolomitization at the Benicàssim outcrop analogue (Maestrat basin, E Spain). Mar. Pet. Geol. 55, 26–42. https://doi.org/10.1016/j.marpetgeo.2013.12.015.
Grandia, F., Cardellach, E., Canals, A., Banks, C.J., 2003. Geochemistry of the fluids related to epigenetic carbonate-hosted Zn-Pb deposits in the Maestrat Basin, Eastern Spain: fluid inclusion and isotope (Cl, C, O, S, Sr) evidence. Econ. Geol. 98, 933–954. https://doi.org/10.2113/gsecongeo.98.5.933.
Gregg, J.M., Sibley, D.F., 1984. Epigenetic dolomitization and the origin of xenotopic dolomite texture. J. Sediment. Petrol. 54, 908–931. https://doi.org/10.1306/212F8A30-2B24-11D7-8648000102C1865D.
Guberman, D.E., 2015. Germanium. U.S. Geological Survey Mineral Commodity Summaries, January 2015. U.S. Geological Survey, Reston, Va, pp. 64–65.
Hao, Z., Chen, H., Xu, F., Wang, Q., 2014. The middle assemblages of fluid inclusions characteristics and significance of dolomite in Majiagou Formation in Ordos Basin, China. Acta Geol. Sin. 88, 1099–1100. https://doi.org/10.1111/1755-6724.12379_19.
Hirani, J., Bastesen, E., Boyce, A., Corlett, H., Eker, A., Gawthorpe, R., Hollis, C., Korneva, I., Rotevatn, A., 2018. Structural controls on non-fabric-selective dolomitization within rift-related basin-bounding normal fault systems: insights from the Hammam Faraun Fault, Gulf of Suez, Egypt. Basin Res. 30 (5), 990–1014. https://doi.org/10.1111/bre.12290.
Hosseini-Dinani, H., Aftabi, A., 2016. Vertical lithogeochemical halos and zoning vectors at Goushfil Zn–Pb deposit, Irankuh district, southwestern Isfahan, Iran: Implications for concealed ore exploration and genetic models. Ore Geol. Rev. 72, 1004–1021. https://doi.org/10.1016/j.oregeorev.2015.09.023.
Hou, Y., Azmy, K., Berra, F., Jadoul, F., Blamey, N.J.F., Gleeson, S.A., Brand, U., 2016. Origin of the Breno and Esino dolomites in the western Southern Alps (Italy): Implications for a volcanic influence. Mar. Pet. Geol. 69, 38–52. https://doi.org/10.1016/j.marpetgeo.2015.10.010.
Huang, S., Huang, K., Lü, J., 2014. The relationship between dolomite textures and their formation temperature: a case study from the Permian-Triassic of the Sichuan Basin and the Lower Paleozoic of the Tarim Basin. Pet. Sci. 11, 39–51. https://doi.org/10.1007/s12182-014-0316-7.
Huang, S., Hou, M., Chen, A., Xu, S., Zhang, B., Deng, Y., Yu, Y., 2022. Fluid properties and genesis of dolomites in the devonian Guanwushan Formation of Upper Yangtze Platform, SW China. Minerals 12, 317. https://doi.org/10.3390/min12030317.
Jaskula, B.W., 2015. Gallium. U.S. Geological Survey Mineral Commodity Summaries, January 2015. U.S. Geological Survey, Reston, Va, pp. 58–59.
Kelley, D.L., Kelley, K.D., Coker, W.B., Caughlin, B., Doherty, M.E., 2006. Beyond the obvious limits of ore deposits: The use of mineralogical, geochemical, and biological features for the remote detection of mineralization. Econ. Geol. 101, 729–752. https://doi.org/10.2113/gsecongeo.101.4.729.
Klinkhammer, G.P., Elderfield, H., Edmond, J.M., Mitra, A., 1994. Geochemical implications of rare earth element patterns in hydrothermal fluids from mid-ocean ridges. Geochim. Cosmochim. Acta 58, 5105–5113. https://doi.org/10.1016/0016-7037(94)90297-6.
Land, L.S., 1983. The application of stable isotope studies of the origin of dolomite and to problems of diagenesis of clastic sediments, in: Arthur, M.A., Anderson, T.F. (Eds.), Stable Isotopes in Sedimentary Geology. Society of Economic Paleontologists and Mineralogists Short Course, pp. 1–22.
Lapponi, F., Casini, G., Sharp, I., Blendinger, W., Fernandez, N., Romaire, I., Hunt, D., 2011. From outcrop to 3D modelling: a case study of a dolomitized carbonate reservoir, Zagros Mountains, Iran, in: Hollis, C., Sharp, I. (Eds.), Albian-Cenomanian-Turonian Carbonate-Siliciclastic Systems of the Arabian Plate; Advances in Diagnosis, Structure and Reservoir Modeling. Petroleum Geoscience, pp. 283–307. https://doi.org/10.1144/1354-079310-040.
Large, R.R., Bull, S.W., Winefield, P.R., 2001. Carbon and oxygen isotope halo in carbonates related to the McArthur River (HYC) Zn-Pb-Ag deposit, north Australia: implications for sedimentation, ore genesis, and mineral exploration. Econ. Geol. 96, 1567–1593. https://doi.org/10.2113/gsecongeo.96.7.1567.
Leach, L.F., Sangster, D.F., 1993. Mississippi Valley-type lead-zinc deposits, in: Kirkham, R.V., Sinclair, W.D., Thorpe, R.I., Duke, J.M. (Eds.), Mineral Deposits Modeling. Geological Association of Canada Special Paper, pp. 289–314.
Leach, D.L., Sangster, D.F.S., Keller, K.D., Large, R.R., Garven, G., Allen, C.R., Gutzmer, J., Walters, S., 2005. Sediment-hosted Lead-Zinc deposits: A global perspective. Economic Geology 100th Anniversary Volume, 561-607.
Li, Q., Jiang, Z., Hu, W., You, X., Hao, G., Zhang, J., Wang, X., 2016. Origin of dolomites in the Lower Cambrian Xiaoerbulak Formation in the Tarim Basin, NW China: Implications for porosity development. J. Asian Earth Sci. 115, 557–570. https://doi.org/10.1016/j.jseaes.2015.10.022.
López-Horgue, M.A., Iriarte, E., Schröder, S., Fernández-Mendiola, P.A., Caline, B., Corneyllie, H., Frémont, J., Sudrie, M., Zerti, S., 2010. Structurally controlled hydrothermal dolomites in Albian carbonates of the Asón valley, Basque Cantabrian Basin, Northern Spain. Mar. Pet. Geol. 27, 1069–1092. https://doi.org/10.1016/j.marpetgeo.2009.10.015.
Loucks, R.R., 2014. Distinctive composition of copper-ore-forming arc magmas. Aust. J. Earth Sci. 61, 5–16. https://doi.org/10.1080/08120099.2013.865676.
Lu, Y.J., Loucks, R.R., Fiorentini, M., McCuaig, T.C., Evans, N.J., Yang, Z.M., Hou, Z.Q., Kirkland, C.L., Parra-Avila, L.A., Kobussen, A., 2016. Zircon composition as pathfinder for porphyry Cu±Mo±Au Deposits. Soc. Econ. Geol. Special Publication 19, 329–347.
Luczaj, J.A., 2006. Evidence against the Dorag (mixing-zone) model for dolomitization along the Wisconsin Arch - A case for hydrothermal diagenesis. Am. Assoc. Pet. Geol. Bull. 90, 1719–1738. https://doi.org/10.1306/01130605077.
Machel, H.G., 2004. Concepts and models of dolomitization: a critical reappraisal, in: Braithwaite, C.J.R., Rizzi, G., Darke, G. (Eds.), The Geometry and Petrogenesis of Dolomite Hydrocarbon Reservoirs, Geological Society Special Publication, 35, 7–63.

Marsh, E.E., Hitzman, M.W., Leach, D.L., 2016. Critical elements in sediment-hosted deposits (Clastic-dominated Zn-Pb-Ag, Mississippi Valley-Type Zn-Pb, Sedimentary rock-hosted stratiform Cu, and Carbonate-hosted polymetallic deposits): A review. Rev. Econ. Geol. 18, 307–321. https://doi.org/10.5382/Rev.18.12.

Martín-Martín, J.D., Gomez-Rivas, E., Bover-Arnal, T., Travé, A., Salas, R., Moreno-Bedmar, J.A., Tomás, S., Corbella, M., Teixell, A., Vergés, J., Stafford, S.L., 2013. The Upper Aptian to Lower Albian syn-rift carbonate succession of the southern Maestrat Basin (Spain): Facies architecture and fault-controlled stratabound dolostones. Cretac. Res. 41, 217–236. https://doi.org/10.1016/j.cretres.2012.12.008.

Martín-Martín, J.D., Travé, A., Gomez-Rivas, E., Salas, R., Sizun, J.P., Vergés, J., Corbella, M., Stafford, S.L., Alfonso, P., 2015. Fault-controlled and stratabound dolostones in the Late Aptian–earliest Albian Benassal formation (Maestrat Basin, E Spain): petrology and geochemistry constrains. Mar. Pet. Geol. 65, 83–102. https://doi.org/10.1016/j.marpetgeo.2015.03.019.

McDonough, W.F., Sun, S.-S., 1995. The composition of the Earth. Chem. Geol. 120, 223–253. https://doi.org/10.1016/0009-2541(94)00140-4.

Migdisov, A.A., Williams-Jones, A.E., Wagner, T., 2009. An experimental study of the solubility and speciation of the rare earth elements (III) in fluoride- and chloride-bearing aqueous solutions at temperatures up to 300°C. Geochim. Cosmochim. Acta 73, 7087–7109. https://doi.org/10.1016/j.gca.2009.08.023.

Muchez, P., Heijlen, W., Banks, D., Blundell, D., Boni, M., Grandia, F., 2005. Extensional tectonics and the timing and formation of basin-hosted deposits in Europe. Ore Geol. Rev. 27, 241–267. https://doi.org/10.1016/j.oregeorev.2005.07.013.

Nader, F.H., Swennen, R., Ellam, R., 2004. Reflux stratabound dolostone and hydrothermal volcanism-associated dolostone: a two-stage dolomitization model (Jurassic, Lebanon). Sedimentology 51, 339–360. https://doi.org/10.1111/j.1365-3091.2004.00629.x.

Naito, K., Fukahori, Y., He, P.M., Sakurai, W., Shimazaki, H., Matsuhisa, Y., 1995. Oxygen and carbon isotope zonations of wall rocks around the Kamioka Pb-Zn skarn deposits, central Japan: Application to prospecting. J. Geochem. Explor. 54, 199–211. https://doi.org/10.1016/0375-6742(95)00044-5.

Navarro-Ciurana, D., Corbella, M., Cardellach, E., Vindel, E., Gómez-Gras, D., Griera, A., 2016a. Petrography and geochemistry of fault-controlled hydrothermal dolomites in the Riópar area (Prebetic Zone, SE Spain). Mar. Pet. Geol. 71, 310–328. https://doi.org/10.1016/j.marpetgeo.2016.01.005.

Navarro-Ciurana, D., Campos-Quispe, L.A., Cardellach, E., Vindel, E., Gómez-Gras, D., Griera, A., Corbella, M., 2016b. Mineralogical and geochemical characterization of the Riópar non-sulfide Zn-(Fe-Pb) deposits (Prebetic Zone, SE Spain). Ore Geol. Rev. 79, 515–532. https://doi.org/10.1016/j.oregeorev.2016.05.023.

Navarro-Ciurana, D., Cardellach, E., Vindel, E., Griera, A., Gómez-Gras, D., Mercè Corbella, M., 2017. Sulfur and lead isotope systematics: Implications for the genesis of the Riópar Zn-(Fe-Pb) carbonate-hosted deposit (Prebetic Zone, SE Spain). Ore Geol. Rev. 91, 928–944. https://doi.org/10.1016/j.oregeorev.2017.08.013.

Navarro-Ciurana, D., Corbella, M., Gómez-Gras, D., Griera, A., Vindel, E., Daniele, L., Cardellach, E. (2015). Relationship between Dolomite Textures and Formation Temperature - Insights from the Riópar Area (Betic basin, SE Spain). European Association of Geoscientists & Engineers. 77th EAGE Conference and Exhibition 2015, 2015, 1–5. https://doi.org/10.3997/2214-4609.201412661.

Nejadhadad, M., Taghipour, B., Zarasvandi, A., Karimzadeh-Somarin, A., 2016. Geological, geochemical, and fluid inclusion evidences for the origin of the Ravanj. Turkish J. Earth Sci. 25, 179–200. https://doi.org/10.3906/yer-1501-26.

Osborne, A.H., Haley, B., Hathorne, E.C., Flögel, S., Frank, M., 2014. Neodymium isotopes and concentrations in Caribbean seawater: tracing water mass mixing and continental input in a semi-enclosed ocean basin. Earth Planet. Sci. Lett. 406, 174–186. https://doi.org/10.1016/j.epsl.2014.09.011.

Pérez-Valera, L.A., Sánchez-Gómez, M., Fernández-Soler, J.M., Pérez-Valera, F., Azor, A., 2010. Diques de lamproítas a lo largo de la falla de Socovos (Béticas orientales). Geogaceta 48, 151–154.

Piepgras, D.J., Jacobsen, S.B., 1992. The behaviour of rare earth elements in seawater: precise determination of variations in the North Pacific water column. Geochim. Cosmochim. Acta 56, 1851–1862. https://doi.org/10.1016/0016-7037(92)90315-A.

Poros, Z., 2011. Fluid Migration and Porosity Evolution in the Buda Hills, Hungary – Selected Examples from Triassic and Paleogene Carbonate Rocks. Tesis Doctoral. Univ. Eötvös Loránd University, p. 155.

Rahim, H., Shah, M.M., Corbella, M., Navarro-Ciurana, M., 2020. Diagenetic evolution and associated dolomitization events in the middle Jurassic Samana Suk Formation, Lesser Himalayan Hill Ranges, NW Pakistan. Carbonates Evaporites 35, 101. https://doi.org/10.1007/s13146-020-00634-0.

Rahim, H., Qamar, S., Shah, M.M., Corbella, M., Martín-Martín, J.D., Janjuhah, H.T., Navarro-Ciurana, D., Lianou, V., Kontakiotis, G., 2022. Processes Associated with Multiphase Dolomitization and Other Related Diagenetic Events in the Jurassic Samana Suk Formation, Himalayan Foreland Basin, NW Pakistan. Minerals 12 (10), 1320. https://doi.org/10.3390/min12101320.

Randazzo, A.F., Zachos, L.G., 1984. Classification and description of dolomite fabrics of rocks from the Floridan aquifer, USA. Sediment. Geol. 37, 151–162. https://doi.org/10.1016/0037-0738(84)90005-8.

Richards, J., 2016. Clues to hidden copper deposits. Nat. Geosci. 9, 195–196. https://doi.org/10.1038/ngeo2656.

Rodríguez-Estrella, T., 1979. Geología e Hidrogeología del Sector de Alcaraz - Liétor - Yeste (Provincia de Albacete). Instituto Geológico i Minero de España 97, 566.

Rodríguez-Pascua, M.A., Calvo, J.P., De Vicente, G., Gómez-Gras, D., 2000. Soft-sediment deformation structures interpreted as seismites in lacustrine sediments of the Prebetic Zone, SE Spain, and their potential use as indicators of earthquake magnitudes during the Late Miocene. Sediment. Geol. 135, 117–135. https://doi.org/10.1016/S0037-0738(00)00067-1.

Ronchi, P., Masetib, D., Tassanc, S., Camocinoa, D., 2012. Hydrothermal dolomitization in platform and basin carbonate successions during thrusting: A hydrocarbon reservoir analogue (Mesozoic of Venetian Southern Alps, Italy). Mar. Pet. Geol. 29, 68–89. https://doi.org/10.1016/j.marpetgeo.2011.09.004.

Sahlström, F., Blake, K., Corral, I., Chang, Z., 2017a. Hyperspectral cathodoluminescence study of indium-bearing sphalerite from the Mt. Carlton high-sulfidation epithermal deposit, Queensland, Australia. Eur. J. Mineral. 29, 985–993. https://doi.org/10.1127/ejm/2017/0029-2660.

Sahlström, F., Arribas, A., Dirks, P., Corral, I., Chang, Z., 2017b. Mineralogical distribution of Germanium, Gallium and Indium at the Mt. Carlton High-Sulfidation Epithermal Deposit, NE Australia, and Comparison with Similar Deposits Worldwide. Minerals, 7, 213. https://doi.org/10.3390/min7110213.

Sanz de Galdeano, C., 1990. Geologic evolution of the Betic Cordilleras in the Western Mediterranean, Miocene to the present. Tectonophysics 172, 107–119. https://doi.org/10.1016/0040-1951(90)90062-D.

Schwarz-Schampera, U., Herzig, P.M., 2002. Indium: Geology, mineralogy, and economics. Springer-Verlag, Heidelberg, p. 258.

Sharp, I., Gillespie, P., Morsalnezhad, D., Taberner, C., Karpuz, R., Vergés, J., Horbury, A., Pickard, N., Garland, J., Hunt, D., 2010. Stratigraphic architecture and fracture-controlled dolomitization of the Cretaceous Khami and Bangestan groups: an outcrop case study, Zagros Mountains, Iran. Geol. Soc. London Spec. Publ. 329, 343–396. https://doi.org/10.1144/SP329.14.

Sibley, D.F., Gregg, J.M., 1987. Classification of dolomite rock textures. J. Sediment. Res. 57, 967–975. https://doi.org/10.1306/212F8CBA-2B24-11D7-8648000102C1865D.

Smith, L.B., Davies, G.R., 2006. Structurally controlled hydrothermal alteration of carbonate reservoirs: introduction. Am. Assoc. Pet. Geol. Bull. 90, 1635–1640. https://doi.org/10.1306/intro901106.

Sverjensky, D.A., 1984. Europium redox equilibria in aqueous solution. Earth Planet. Sci. Lett. 67, 70–78. https://doi.org/10.1016/0012-821X(84)90039-6.

Tan, Q.-P., Xia, Y., Wang, X., Xie, Z.-J., Dong-Tian Wei, D.-T., 2017. Carbon-oxygen isotopes and rare earth elements as an exploration vector for Carlin-type gold deposits: A case study of the Shuiyindong gold deposit, Guizhou Province. SW China. J. Asian Earth Sci. 148, 1–12. https://doi.org/10.1016/j.jseaes.2017.08.013.

Taylor, S.R., McLennan, S.M., 1985. The Continental Crust; its Composition and Evolution. Blackwell, Oxford, p. 312.

Tolcin, A. C., 2015. Indium, in: U.S. Geological Survey Mineral Commodity Summaries, January 2015. U.S. Geological Survey, Reston, Va. pp. 74–75.

Tortola, M., Al-Aasm, I.S., Crowe, R., 2020. Diagenetic pore fluid evolution and dolomitization of the silurian and devonian carbonates, Huron Domain of Southwestern Ontario: petrographic, geochemical and fluid inclusion evidence. Minerals 10, 140. https://doi.org/10.3390/min10020140.

Vázquez, R., Vennemann, T.W., Kesler, S.E., Russell, N., 1998. Carbon and oxygen isotope halos in the host limestone, El Mochito Zn-Pb-(Ag) skarn massive sulfide-oxide deposit. Honduras. Econ. Geol. 93, 15–31. https://doi.org/10.2113/gsecongeo.93.1.15.

Veizer, J., Ala, D., Azmy, K., Bruckschen, P., Buhl, D., Bruhn, F., Carden, G.A.F., Diener, A., Ebneth, S., Godderis, Y., Jasper, T., Korte, C., Pawellek, F., Podlaha, O.G., Strauss, H., 1999. $^{87}Sr/^{86}Sr$, $\delta^{13}C$ and $\delta^{18}O$ evolution of Phanerozoic seawater. Chem. Geol. 161, 59–88. https://doi.org/10.1016/S0009-2541(99)00081-9.

Vera, J.A., Arias, C., García-Hernández, M., López-Garrido, A.C., Martín-Algarra, A., Martín-Chivelet, J., Molina, J.M., Rivas, P., Ruiz-Ortiz, P.A., Sanz de Galdeano, C., Vilas, L., 2004. Las zonas externas béticas y el paelomargen sudibérico, in: Vera, J.A. (Ed.), Geología de España. Sociedad Geológica de España e Instituto Geológico de España, pp. 354–360.

Vilas, L., Dabrio, C., Peláez, J.R., García-Hernández, M., 2001. Dominios sedimentarios generados durante el periodo extensional Cretácico Inferior entre Cazorla y Hellín (Béticas Externas). Su implicación en la estructural actual. Rev. Soc. Geol. España 14, 113–122.

Wang, L., Hu, X., Wang, X., Cao, J., Chen, Q., 2014. Seawater normalized REE patterns of dolomites in Geshan and Panlongdong sections, China: Implications for tracing dolomitization and diagenetic fluids. Mar. Pet. Geol. 56, 63–73. https://doi.org/10.1016/j.marpetgeo.2014.02.018.

Warren, J., 2000. Dolomite: occurrence, evolution and economically important associations. Earth-Science Rev. 52, 1–81. https://doi.org/10.1016/S0012-8252(00)00022-2.

Wilkinson, J.J., Chang, Z., Cooke, D.R., Baker, M.J., Wilkinson, C.C., Inglis, S., Chen, H., Gemmell, J.B., 2015. The chlorite proximitor: A new tool fro detecting porphyry ore deposits. J. Geochem. Explor. 152, 10–26. https://doi.org/10.1016/j.gexplo.2015.01.005.

Wilkinson, J.J., 2014. Sediment-hosted Zinc-Lead Mineralization: Processes and Perspectives. Treatise on Geochemistry, Elsevier, H Holland, K Turekian (ed), Amsterdam, Netherlands, pp. 219-249.

Williams-Jones, A.E., Migdisov, A.A., Samson, I.M., 2012. Hydrothermal mobilisation of the rare earth elements – a tale of "Ceria" and "Yttria". Elements 8, 355–360. https://doi.org/10.2113/gselements.8.5.355.

Wilson, M.E.J., Evans, M.J., Oxtoby, N.H., Nas, D.S., Donnelly, T., Thirlwall, M., 2007. Reservoir quality, textural evolution, and origin of fault-associated dolomites. Am. Assoc. Pet. Geol. Bull. 91 (9), 1247–1272. https://doi.org/10.1306/05070706052.

Xiang, P., Ji, H., Shi, Y., Huang, Y., Sun, Y., Xu, X., Shuqi Zou, S., 2020. Petrographic, rare earth elements and isotope constraints on the dolomite origin of Ordovician Majiagou Formation (Jizhong Depression, North China). Mar. Pet. Geol. 117, 104374 https://doi.org/10.1016/j.marpetgeo.2020.104374.

Xuefeng, Z., Wenxuan, H., Zhijun, J., Juntao, Z., Yixiong, Q., Jingquan, Z., Dongya, Z., Xiaolin, W., Xiaomin, X., 2008. REE Compositions of Lower Ordovician Dolomites in Central and North Tarim Basin, NW China: A Potential REE Proxy for Ancient

Seawater. Acta Geol. Sin. 82, 610–621. https://doi.org/10.1111/j.1755-6724.2008.tb00611.x.

Yesares, L., Drummond, D.A., Hollis, S.P., Doran, A.L., Menuge, J.F., Boyce, A.J., Blakeman, R.J., Ashton, J.H., 2019. Coupling mineralogy, textures and radiogenic isotopes in identifiying ore-forming processes in irish-type carbonate-hosted Zn-Pb deposits. Minerals 9, 335. https://doi.org/10.3390/min9060335.

Zenger, D.H., Dunham, J.B., Ethington, R.L., 1980. Concepts and models of dolomitization. Soc. Econ. Paleontol. Mineral. Spec. Publ. 28, 426.

Zhao, H., Jones, B., 2013. Distribution and interpretation of rare earth elements and yttrium in Cenozoic dolostones and limestones on Cayman Brac, British West Indies. Sediment Geol 284–285, 26–38. https://doi.org/10.1016/j.sedgeo.2012.10.009.

Zheng, Y.F., Hoefs, J., 1993. Carbon and oxygen isotopic covariations in hydrothermal calcites: theoretical modeling on mixing processes and application to Pb-Zn deposits in the Harz Mountains, Germany. Miner. Depos. 28, 79–89. https://doi.org/10.1007/BF00196332.